The dynamics of stellar disks in live dark-matter halos

M. S. Fujii[1]⋆, J. Bédorf[2], J. Baba[3], and S. Portegies Zwart[2]

[1]*Department of Astronomy, Graduate School of Science, The University of Tokyo, 7-3-1 Hongo, Bunkyo-ku, Tokyo, 113-0033, Japan*
[2]*Leiden Observatory, Leiden University, NL-2300RA Leiden, The Netherlands*
[3]*National Astronomical Observatory of Japan, Mitaka-shi, Tokyo 181-8588, Japan*

ABSTRACT

Recent developments in computer hardware and software enable researchers to simulate the self-gravitating evolution of galaxies at a resolution comparable to the actual number of stars. Here we present the results of a series of such simulations. We performed *N*-body simulations of disk galaxies with between 100 and 500 million particles over a wide range of initial conditions. Our calculations include a live bulge, disk, and dark matter halo, each of which is represented by self-gravitating particles in the *N*-body code. The simulations are performed using the gravitational *N*-body tree-code `Bonsai` running on the Piz Daint supercomputer. We find that the time scale over which the bar forms increases exponentially with decreasing disk-mass fraction and that the bar formation epoch exceeds a Hubble time when the disk-mass fraction is ~ 0.35. These results can be explained with the swing-amplification theory. The condition for the formation of $m = 2$ spirals is consistent with that for the formation of the bar, which is also an $m = 2$ phenomenon. We further argue that the non-barred grand-design spiral galaxies are transitional, and that they evolve to barred galaxies on a dynamical timescale. We also confirm that the disk-mass fraction and shear rate are important parameters for the morphology of disk galaxies. The former affects the number of spiral arms and the bar formation epoch, and the latter determines the pitch angle of the spiral arms.

Key words: galaxies: kinematics and dynamics — galaxies: spiral — galaxies: structure — galaxies: evolution — methods: numerical

1 INTRODUCTION

Simulations serve as a powerful tool to study the dynamical evolution of galaxies. Galaxies are extremely complicated, in particular due to the coupling between a varying environment and their internal evolution. Even the relatively simple self-gravity of an isolated galaxy poses enormous challenges, in particular because of the non-linear processes that govern the formation of spiral arms and bar-like structures. Many of these processes have been attributed to perturbations from outside, and it is not a priori clear to what extent internal dynamical processes play a role in the formation of axis-asymmetric structures in disk galaxies. Self-gravitating disks are prone to form spiral arms and/or bars, but the precise conditions under which these form are not well understood.

In earlier simulations Hohl (1971) demonstrated, using $\sim 7 \times 10^4$ cells with near-neighbour interactions, that a stellar disk without a (dark matter) halo leads to the formation of a bar within a few galactic rotations. In a subse-

quent study Ostriker & Peebles (1973) concluded that a dark-matter halo is required to keep the disk stable. For spiral galaxies, Sellwood & Carlberg (1984) performed simulations of two-dimensional stellar disks with ~ 7000 cells and 2×10^4 particles that developed multiple spiral arms. They suggested that spiral arms tend to kinematically heat-up the disk, and that in the absence of an effective coolant, such as ambient gas or star formation, this heating would cause the spiral structures to disappear within a few galactic rotations. Carlberg & Freedman (1985) also performed a series of simulations and found that the number of spiral arms decrease as the disk-to-halo mass ratio decreases. In contradiction to the Lin-Shu quasi-stationary density-wave theory (Lin & Shu 1964), these simulations suggested that spiral arms are transient and develop from small perturbations amplified by the self-gravity in a differentially rotating disk (Goldreich & Lynden-Bell 1965; Julian & Toomre 1966). Today this mechanism is known as "swing amplification" (Toomre 1981; Michikoshi & Kokubo 2016b).

The number of particles in simulations has gradually increased with time as computers have become more powerful.

⋆ E-mail: fujii@astron.s.u-tokyo.ac.jp (MSF)

After Sellwood & Carlberg (1984) and Carlberg & Freedman (1985), the formation and evolution of bar structures were often studied using three dimensional N-body simulations. Combes et al. (1990) showed that bars induce a peanut-shaped (boxy) bulge using a three-dimensional Particle-Mesh method with at most $\sim 8 \times 10^6$ cells. N-body simulations with up to 2^8 particles were performed by Sellwood & Carlberg (2014), but they adopted a rigid potential for the dark matter halo. Performing such simulations with a 'live' particle halo has been hindered by the sheer computer power needed to resolve baryonic and non-baryonic material simultaneously.

The importance of resolving the halo in such simulations using particles was emphasized by Athanassoula (2002). They found that once a bar formed its angular momentum is transferred to the halo. This angular momentum transport can only be resolved in the simulations if the halo is represented by particles that are integrated together with the rest of the galaxy. The dynamics and back-coupling of such a live halo also affects the evolution of the bar. In this study, we adopt a tree method (Barnes & Hut 1986) for solving the equations of motion of all particles in the simulations. Several other simulations of barred galaxies, in which halos were resolved using live particles, also adopted a tree-code (Widrow & Dubinski 2005; Widrow et al. 2008). Dubinski et al. (2009) performed a series of such N-body simulations with up to 10^8 particles. They confirmed that such a large number of particles is required but also sufficient to obtain a reliable solution for the morphology of the bar. However, they also found that bar formation in simulations with a larger number of particles was systematically delayed.

Another problem of relatively low-resolution is the artificial heating of the particles by close encounters. In simulations of spiral galaxies with multiple arms, Fujii et al. (2011) demonstrated that this effect becomes sufficiently small when the disk is resolved with at least one million particles. If a galactic disk needs to be resolved with at least a million particles, it is understandable that simulating an entire galaxy, including the dark matter halo, would require at least 10 times this number in order to properly resolve the disk and halo in an N-body simulation. To overcome the numerical limitations researchers tend to adopt a rigid background potential for the galaxy's dark matter halo. (e.g., Sellwood & Carlberg 1984; Baba et al. 2013; Grand et al. 2013), as was also done in Fujii et al. (2011). In these simulations energy cannot be transported self-consistently between the halo and the disk, and vice versa. Taking this coupling into account is particularly relevant when studying the formation and evolution of non-axisymmetric structures such as spiral arms and a bar in the disk; bars tend to slow down due to angular-moment transfer with the halo and grow faster when compared to models with a rigid halo (Athanassoula 2002).

Up to now it has not been possible to carry out extensive parameter searches with a sufficient number of particles that include a live halo, simply because the amount of computer time required for such studies exceeds the hardware and software capacity (e.g. Dubinski et al. 2009). The current generation of GPU-based supercomputers and optimized N-body algorithms Portegies Zwart & Bédorf (2015) allows us to perform simulations with more than a hundred billion particles (Bédorf et al. 2014) over a Hubble time.

The same developments allow us to perform an extensive parameter over a wide range of initial conditions with a more modest number of particles.

We developed the gravitational tree-code `Bonsai` to perform such simulations. `Bonsai`, uses the GPUs to accelerate the calculations and achieves excellent efficiency with up to ~ 19000 GPUs (Bédorf et al. 2012, 2014). The efficiency of `Bonsai` allows us to run simulations with a hundred million particles for 10 Gyr in a few hours using 128 GPUs in parallel. This development allows us to perform simulations of disk galaxies for the entire lifetime of the disk, and therefore to study the formation of structure using a realistic resolution and time scale. The code is publicly available and part of the `AMUSE` framework (Portegies Zwart & McMillan 2018).

Using `Bonsai` running on the CSCS Piz Daint supercomputer we performed a large number of disk galaxy simulations with live dark-matter halos at a sufficiently high resolution to suppress numerical heating on the growth of the physical instabilities due to the self-gravity of the disk. With these simulations, we study the relation between the initial conditions and the final disk galaxies.

2   *N*-BODY SIMULATIONS

We performed a series of N-body simulations of galactic stellar disks embedded in dark matter halos. In this section, we describe our choice of parameters and the N-body code used for these simulations.

2.1   Model

Our models are based on those described in Widrow et al. (2008) and Widrow & Dubinski (2005). We generated the initial conditions using GalactICS (Widrow & Dubinski 2005). The initial conditions for generating the dark mater halo are taken from the NFW profile (Navarro et al. 1997), which has a density profile following:

$$\rho_{\mathrm{NFW}}(r) = \frac{\rho_{\mathrm{h}}}{(r/a_{\mathrm{h}})(1+r/a_{\mathrm{h}})^3}, \tag{1}$$

and the potential is written as

$$\Phi_{\mathrm{NFW}} = -\sigma_{\mathrm{h}}^2 \frac{\log(1+r/a_{\mathrm{h}})}{r/a_{\mathrm{h}}}. \tag{2}$$

Here the gravitational constant, G, is unity, a_{h} is the scale radius, $\rho_{\mathrm{h}} \equiv \sigma^2/4\pi a_{\mathrm{h}}^2$ is the characteristic density, and σ_{h} is the characteristic velocity dispersion. We adopt $\sigma_{\mathrm{h}} = 340$ (km s^{-1}), $a_{\mathrm{h}} = 11.5$ (kpc). Since the NFW profile is infinite in extent and mass, the distribution is truncated by a halo tidal radius using an energy cutoff $E_{\mathrm{h}} \equiv \varepsilon_{\mathrm{h}} \sigma_{\mathrm{h}}^2$, where ε_{h} is the truncation parameter with $0 < \varepsilon_{\mathrm{h}} < 1$. Setting $\varepsilon_{\mathrm{h}} = 0$ yields a full NFW profile (see Widrow & Dubinski 2005, for details). We choose the parameters of the dark matter halo such that the resulting rotation curves have a similar shape. The choice of parameters is summarized in Table 1.

For some models we assume the halo to have net angular momentum. This is realized by changing the sign of the angular momentum about the symmetry axis (J_z). The rotation is parameterized using α_{h}. For $\alpha_{\mathrm{h}} = 0.5$, the fraction of halo particles which have positive or negative J_z are the same, in which case the disk has no net angular momentum. If $\alpha_{\mathrm{h}} > 0.5$, the halo rotates in the same direction as the disk.

For the disk component, we adopt an exponential disk for which the surface density distribution is given by

$$\Sigma(R) = \Sigma_0 e^{-R/R_d}. \tag{3}$$

The vertical structure is given by $\text{sech}^2(z/z_d)$, where z_d is the disk scale height. The radial velocity dispersion is assumed to follow $\sigma_R^2(R) = \sigma_{R0}^2 \exp(-R/R_d)$, where σ_{R0} is the radial velocity dispersion at the disk's center. Toomre's stability parameter Q (Toomre 1964; Binney & Tremaine 2008) at a reference radius (we adopt $2.2R_d$), Q_0, is controlled by the central velocity dispersion of the disk (σ_{R0}). We tune σ_{R0} such that for our standard model (md1mb1) $Q_0 = 1.2$.

For model md1mb1 we use as disk mass $M_d=4.9 \times 10^{10}$ $M_\odot$, and the scale length $R_d=2.8$ kpc. The disk's truncation radius is set to 30 kpc, the scale height $z_d=0.36$ kpc and the radial velocity dispersion at the center of the galaxy to $\sigma_{R0}=105$ km s^{-1}. The disk is truncated at (R_{out}) with a radial range for disk truncation (δR). We adopt $R_{\text{out}} = 30.0$ (kpc) and $\delta R = 0.8$ (kpc).

For the bulge we use a Hernquist model (Hernquist 1990), but the distribution function is extended with an energy cutoff parameter (ε_b) to truncate the profile much in the same way as we did with the halo model. The density distribution and potential of the standard Hernquist model is

$$\rho_H = \frac{\rho_b}{(r/a_b)(1+r/a_b)^3} \tag{4}$$

and

$$\Phi_H = \frac{\sigma_b^2}{1+r/a_b}. \tag{5}$$

Here a_b, $\rho_b = \sigma_b^2/(2\pi a_b^2)$, and σ_b are the scale length, characteristic density, and the characteristic velocity of the bulge, respectively. We set $\sigma_b=300$ km s^{-1}, bulge scale length $a_b=0.64$ kpc, and the truncation parameter ($\varepsilon_b=0.0$). This results in a bulge mass of $4.6 \times 10^9 M_\odot$, which is consistent with the Milky Way model proposed by Shen et al. (2010), and reproduces the bulge velocity distribution obtained by BRAVA observations (Kunder et al. 2012). We do not assume an initial rotational velocity for the bulge.

For the simulation models we vary the disk mass, bulge mass, scale length, halo spin, and Q_0. Since the adopted generator for the galaxies is an irreversible process and due to the randomization of the selection of particle positions and velocities we cannot guarantee that the eventual velocity profile is identical to the input profile, but we confirmed by inspection that they are indistinguishable. The initial conditions for each of the models are summarized in Table 1. The mass and tidal radius for the bulge, disk, and halo as created by the initial condition generator are given in Table 2.

In each of the models we fix the number of particles used for the disk component to 8.3×10^6. For the bulge and halo particles we adopt the same particle mass as for the disk particles. As a consequence the mass ratios between the bulge, halo and disk are set by having a different number of particles used per component (Table 2).

2.2 The `Bonsai` optimized gravitational *N*-body tree-code

We adopted the `Bonsai` code for all calculations (Bédorf et al. 2012, 2014). `Bonsai` implements the classical Barnes & Hut algorithm (Barnes & Hut 1986) but then optimized for Graphics Processing Units (GPU) and massively parallel operations. In `Bonsai` all the compute work, including the tree-construction, takes place on the GPU which frees up the CPU for administrative tasks. By moving all the compute work to the GPU there is no need for expensive data copies, and we take full advantage of the large number of compute cores and high memory bandwidth that is available on the GPU. The use of GPUs allows fast simulations, but we are limited by the relatively small amount of memory on the GPU. To overcome this limitation we implemented across-GPU and across-node parallelizations which enable us to use multiple GPUs in parallel for a single simulation (Bédorf et al. 2014). Combined with the GPU acceleration, this parallelization method allows `Bonsai` to scale efficiently from single GPU systems all the way to large GPU clusters and supercomputers (Bédorf et al. 2014). We used the version of `Bonsai` that incorporates quadrupole expansion of the multipole moments and the improved Barnes & Hut opening angle criteria (Iannuzzi & Athanassoula 2013). We use a shared time-step of ~ 0.6 Myr, a gravitational softening length of 10 pc and the opening angle $\theta = 0.4$.

Our simulations contain hundreds of millions of particles and therefore it is critical that the post-processing is handled efficiently. We therefore implemented the post-processing methods directly in `Bonsai` and these are executed while the simulation is progressing. This eliminates the need to reload snapshot data (which can be on the order of a few terabytes) after the simulation.

The simulations in this work have been run on the Piz Daint supercomputer at the Swiss National Supercomputing Centre. In this machine each compute node contains an NVIDIA Tesla K20x GPU and an Intel Xeon E5-2670 CPU. Depending on the number of particles in the simulation we used between 8 and 512 nodes per simulation.

3 RESULTS

3.1 The effects of disk and bulge masses

We study the effect that the disk and bulge mass fractions have on the halo and on the morphology of spiral arms and bars. In Fig. 1, we summarize the initial rotation curves of several models: models md1mb1, md0.5mb1, md0.3mb1, and md0.1mb1 (varying disk mass) and models md0.5mb0 and md0.5mb3 (varying bulge mass). We present the snapshots at $t = 5$ and 10 Gyr in Figs. 2 and 3. As reported in previous studies, the number of spiral arms increase as the disk mass decreases (Carlberg & Freedman 1985; Bottema 2003; Fujii et al. 2011; D'Onghia 2015) and the formation of the bar is delayed when the bulge mass is increased (Saha & Naab 2013). This corresponds to the effect that centrally concentrated potentials prevent the formation of bars (Sellwood & Evans 2001).

Table 1. Model names and their parameters. The columns represent, 1: Model name, 2: Halo scale radius, 3: Halo characteristic velocity dispersion, 4: Halo truncation parameter, 5: Halo rotation parameter, 6: Disk mass, 7: Disk scale radius, 8: Disk scale height, 9: Disk radial velocity dispersion at the center of the disk, 10: Bulge scale length, 11: Bulge characteristic velocity, 12: Bulge truncation parameter. In the model names, 'md' and 'mb' indicate disk and bulge masses. 'Rd' and 'rb' indicate the disk and halo scale radii. 's' indicates models with halo spin. 'Q' indicates the initial Q value. For these, the values of model md1mb1 are referred to as 1. For all models, movies of the evolution are available in the online materials.

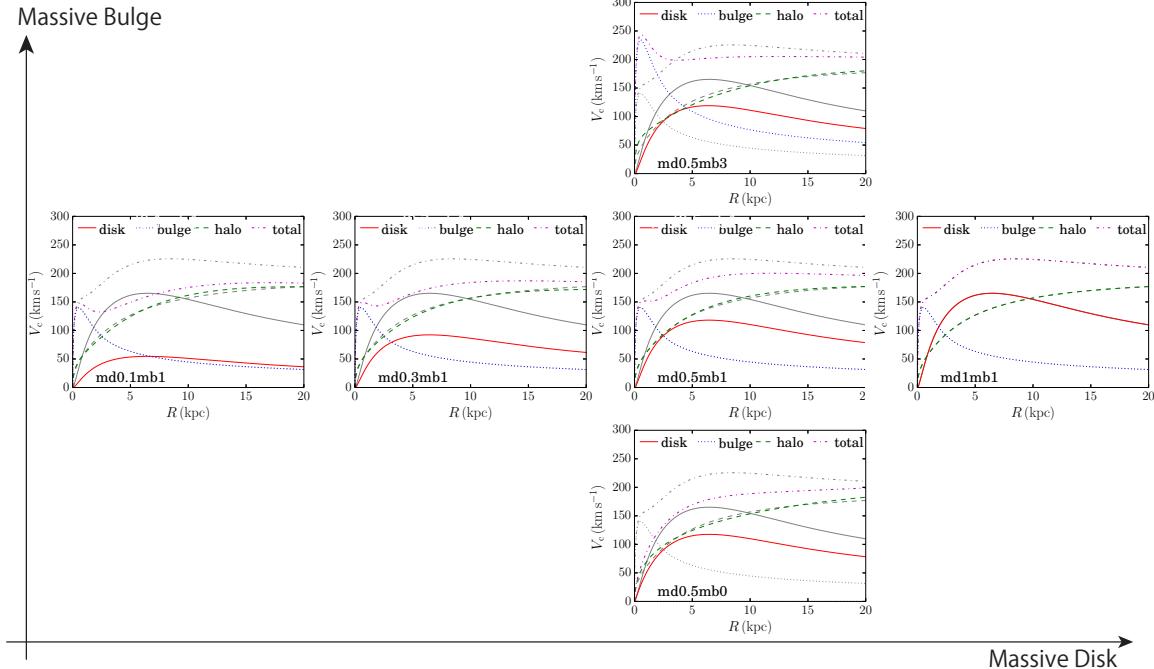| (1)	(2)	(3)	(4)	(5)	(6)	(7)	(8)	(9)	(10)	(11)	(12)
	Halo				Disk				Bulge		
Parameters	a_h	σ_h	$1-\varepsilon_h$	α_h	M_d	R_d	z_d	σ_{R0}	a_b	σ_b	$1-\varepsilon_b$
Model	(kpc)	(km s^{-1})			($10^{10}M_\odot$)	(kpc)	(kpc)	(km s^{-1})	(kpc)	(km s^{-1})	
md1mb1	11.5	340	0.8	0.5	4.9	2.8	0.36	105	0.64	300	1.0
md1mb1s0.65	11.5	340	0.8	0.65	4.9	2.8	0.36	105	0.64	300	1.0
md1mb1s0.8	11.5	340	0.8	0.8	4.9	2.8	0.36	105	0.64	300	1.0
md0.5mb1	8.2	310	0.88	0.5	2.5	2.8	0.36	59.2	0.64	300	0.86
md0.4mb1	7.6	300	0.91	0.5	2.0	2.8	0.36	49.0	0.64	300	0.84
md0.3mb1	7.0	287	0.92	0.5	1.5	2.8	0.36	38.5	0.64	300	0.82
md0.1mb1	6.0	285	0.97	0.5	0.49	2.8	0.36	13.5	0.64	300	0.79
md0.5mb0	22.0	450	0.7	0.5	2.3	2.8	0.36	62.6	0.64	500	0.86
md0.5mb3	7.0	270	0.8	0.5	2.3	2.8	0.36	59.0	0.64	500	0.79
md0.5mb4	6.6	260	0.82	0.5	2.3	2.8	0.36	58.3	0.64	545	0.80
md0.5mb4rb3	13.5	360	0.8	0.5	2.3	2.8	0.36	57.2	1.92	380	0.99
md1mb1Rd1.5	9.0	290	0.95	0.5	4.9	4.2	0.36	74.2	0.64	300	0.85
md0.5mb1Rd1.5	7.5	290	0.91	0.5	2.5	4.2	0.36	39.8	0.64	300	0.8
md0.5Rmb1d1.5s	7.5	290	0.91	0.8	2.5	4.2	0.36	39.8	0.64	300	0.8
md1.5mb5	13.0	280	0.9	0.5	7.3	2.8	0.36	138	1.0	550	0.8
md1mb10	18.0	500	0.9	0.5	4.9	2.8	0.36	93.2	1.5	600	1.0
md0.5mb0Q0.5	22.0	450	0.7	0.5	2.3	2.8	0.36	26.1	0.64	500	0.86
md0.5mb0Q2.0	22.0	450	0.7	0.5	2.3	2.8	0.36	105	0.64	500	0.86

Figure 1. Rotation curves of the initial conditions for models md1mb1, md0.5mb1, md0.3mb1, md0.1mb1, md0.5mb0, and md0.5mb3. The gray solid, dotted, dashed, and dot-dashed curves indicate disk, bulge, halo, and total rotation curves of model md1mb1.

Table 2. Models: mass, radius, and number of particles per component. Column 1: Model name, 2: Disk mass, 3: Bulge mass, 4: Halo mass, 5: Disk outer radius, 6: Bulge outer radius, 7: Halo outer radius, 8: Toomre's Q value at the reference point ($2.2R_d$), 9: Bulge-to-disk mass ratio (B/D), 10: Number of particles for the disk, 11: Number of particles for the bulge, 12: Number of particles for the halo.

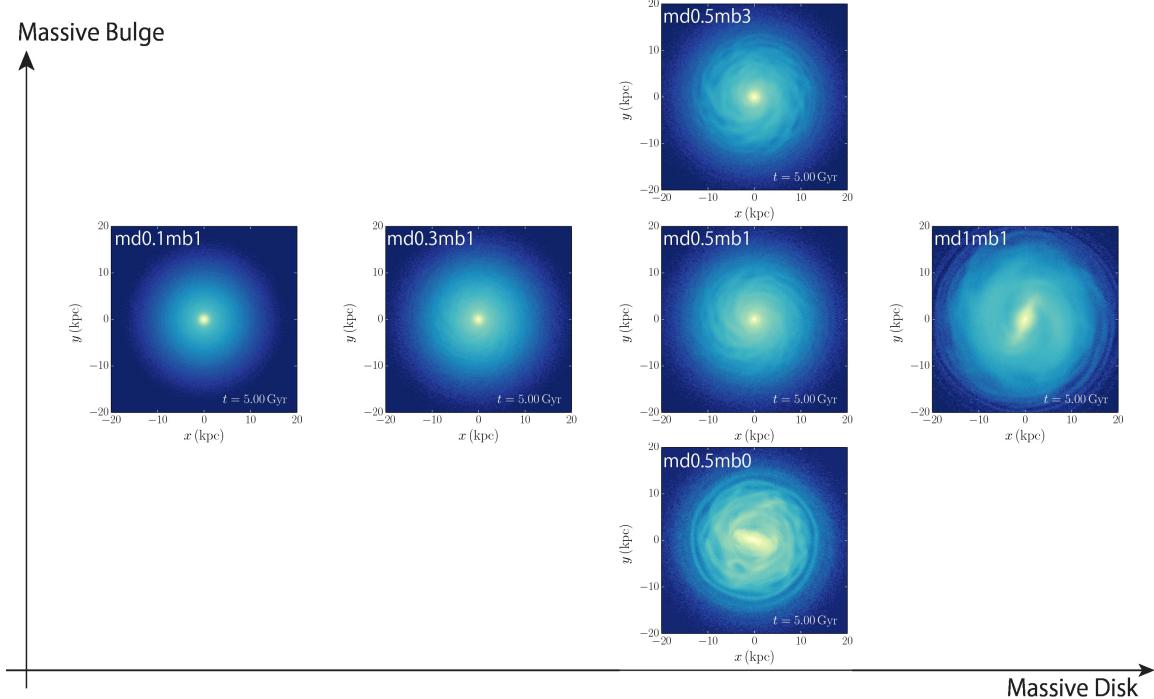| (1) Model	(2) M_d $(10^{10}M_\odot)$	(3) M_b $(10^{10}M_\odot)$	(4) M_h $(10^{10}M_\odot)$	(5) $R_{d,t}$ (kpc)	(6) $r_{b,t}$ (kpc)	(7) $r_{h,t}$ (kpc)	(8) Q_0	(9) M_b/M_d	(10) N_d	(11) N_b	(12) N_h
md1mb1	4.97	0.462	59.7	31.6	3.17	229	1.2	0.0930	8.3M	0.77M	100M
md1mb1s0.65	4.97	0.462	59.7	31.6	3.17	229	1.2	0.0930	8.3 M	0.77M	100M
md1mb1s0.8	4.97	0.462	59.7	31.6	3.17	229	1.2	0.0930	8.3M	0.77M	100M
md0.5mb1	2.55	0.465	43.8	31.6	2.56	232	1.2	0.182	8.3M	1.5M	140M
md0.4mb1	2.05	0.463	41.4	31.6	2.52	261	1.2	0.226	8.3M	1.9M	170M
md0.3mb1	1.56	0.462	36.2	31.6	2.49	247	1.2	0.296	8.3M	2.5M	190M
md0.1mb1	0.546	0.466	33.3	31.6	2.44	340	1.2	0.853	8.3M	7.1M	510M
md0.5mb0	2.53	0.0	100.0	31.6	-	295	1.2	0.00	8.3M	-	330M
md0.5mb3	2.61	1.37	39.7	31.6	2.81	120	1.2	0.525	8.3M	4.4M	130M
md0.5mb4	2.62	1.69	41.4	31.6	2.96	125	1.2	0.645	8.3M	5.4M	130M
md0.5mb4rb3	2.60	1.76	86.7	31.6	8.55	229	1.2	0.676	8.3M	5.4M	130M
md1mb1Rd1.5	5.06	0.464	47.1	46.6	2.61	620	1.2	0.0916	8.3M	0.77M	78M
md0.5mb1Rd1.5	2.59	0.457	35.2	46.6	2.47	249	1.2	0.176	8.3M	1.5M	110M
md0.5mb1Rd1.5s	2.59	0.457	35.2	46.6	2.47	249	1.2	0.176	8.3M	1.5M	110M
md1.5mb5	7.52	2.09	104.6	31.6	3.53	269	1.2	0.279	8.3M	2.3M	120M
md1mb10	5.17	5.22	2050	31.6	11.6	264	1.2	1.0	8.3M	8.4M	400M
md0.5mb1Q0.5	2.55	0.465	43.8	31.6	2.56	232	0.5	0.182	8.3M	1.5M	140M
md0.5mb1Q2.0	2.55	0.465	43.8	31.6	2.56	232	2.0	0.182	8.3M	1.5M	140M

Figure 2. Snapshots (surface densities) at $t = 5$ Gyr for models md1mb1, md0.5mb1, md0.3mb1, md0.1mb1, md0.5mb0, and md0.5mb3.
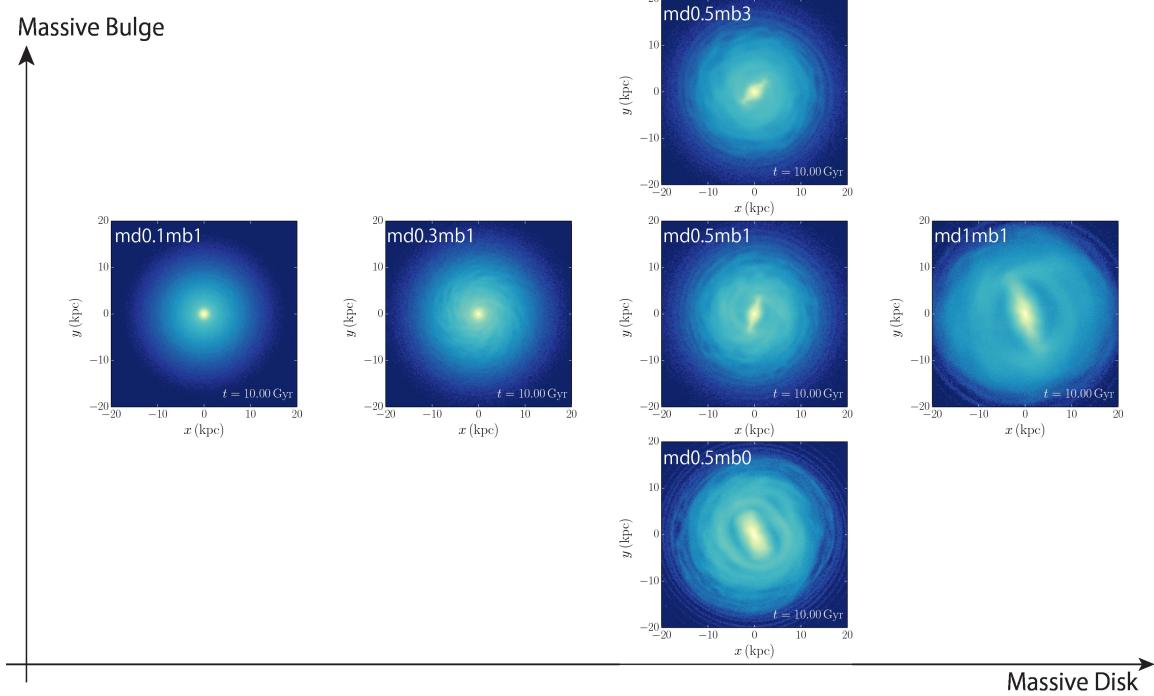
Figure 3. Snapshots (surface densities) at $t = 10$ Gyr for models md1mb1, md0.5mb1, md0.3mb1, md0.1mb1, md0.5mb0, and md0.5mb3.

3.2 Spiral Arms

3.2.1 Number of Spiral Arms

We first focus on the number of spiral arms. As is shown in Fig. 3, the number of spiral arms increases as the disk mass decreases. This relation can be understood by swing amplification theory (Toomre 1981). In a differentially rotating disk, the epicycle motions of particles are amplified and the amplification factor X is written as

$$X \equiv \frac{k_{\mathrm{crit}}R}{m} = \frac{\kappa^2 R}{2\pi G\Sigma m}. \tag{6}$$

Here R is the distance from the galactic center and m is the spiral multiplicity (the number of spiral arms). This m is usually used for spirals, we adopt $m = 2$ for bars, because bars are traced as a $m = 2$ mode when using a Fourier decomposition. For typical disk models the amplification is large for $1 \lesssim X \lesssim 2$ and rapidly drops for $2 \lesssim X \lesssim 3$ (Goldreich & Lynden-Bell 1965; Julian & Toomre 1966; Toomre 1981). The critical wave number k_{crit} (and also the critical wave length λ_{crit}) is obtained from the local stability in a razor-thin disk using the tight-winding approximation (Toomre 1964):

$$k_{\mathrm{crit}} = \frac{\kappa^2}{2\pi G\Sigma}, \tag{7}$$

$$\lambda_{\mathrm{crit}} = \frac{2\pi}{k_{\mathrm{crit}}} = \frac{4\pi^2 G\Sigma}{\kappa^2}, \tag{8}$$

where Σ and κ are the surface density and the epicyclic frequency of the disk, respectively (see also section 6.2.3 of Binney & Tremaine 2008).

Equation (6) also predicts the number of spiral arms that form in a disk. By inverting equation (6) one obtains a

relation for m as a function of the swing amplification factor X:

$$m = \frac{\kappa^2 R}{2\pi G\Sigma X}. \tag{9}$$

Because the perturbations grow most efficiently for $X \sim 1$–2, we can relate m as a function of R (here, both κ and Σ are written as a function of R.). The predicted number of spiral arms from swing amplification theory has been validated using numerical simulations (Carlberg & Freedman 1985; D'Onghia 2015).

For models with different disk masses, we estimate the number of spiral arms using equation (9) and present the results in Fig. 4. The dashed curves present the estimated number of spiral arms as a function of galactic radii where we adopt $X \sim 2$ following Carlberg & Freedman (1985); Dobbs & Baba (2014). Given the curves we expect fewer arms for the more massive models and the number of arms increases for larger radii (R).

We also determine the number of spiral arms for each of the simulated galaxies and overplot the results in Fig. 4. We use a Fourier decomposition of the disks surface density:

$$\frac{\Sigma(R, \phi)}{\Sigma_0(R)} = \sum_{m=0}^{\infty} A_m(R) e^{im[\phi - \phi_m(R)]}, \tag{10}$$

where $A_m(R)$ and $\phi_m(R)$ are the Fourier amplitude and phase angle for the m-th mode at R, respectively. We measure the amplitude at each radius up to 20 kpc using radial bins of $\Delta R = 1$ kpc. When a bar formed we obtained $m = 2$ as strongest amplitude.

Because the spiral arms are transient structures the dominant number of spiral arms, those with the highest amplitude, changes over time (Fujii et al. 2011). We therefore use the most frequently appearing number of spiral arms

(hereafter, principal mode) as the number of arms (m) of the model. The principal mode is measured between 2.5 and 14.5 kpc at 2 kpc intervals, and for each the 1000 snapshots between 0 and 10 Gyr. The results are presented in Fig. 4. The $m = 2$ mode will always become the dominant mode once a bar has formed (see red circles in the figure), but spiral arms might have formed before the bar formation. We therefore also show the principal mode before the bar formation (triangular symbols). These results are roughly consistent with the number of spiral arms predicted by Eq. 9: the number of spiral arms increases as the galactic radius increases and as the disk mass decreases. For model md0.1mb1 we measure a principal mode of 2 at $R = 6.5$ kpc. However, when we look at Fig. 3, we see more than 2 faint spiral arms. We therefore also measured the strongest modes excluding $m = 2$. These modes are indicated by the square symbols. We perform the same analysis for all the other models and measure the number of spiral arms (for the details of the individual evolution of these models, see the following sections and Appendix B). The results are summarized in Table 3.

Numerical results tend to deviate from theoretical predictions as the number of spiral arms increases. The more spiral arms the fainter they become, which makes them harder to measure and identify in the simulations. Our method has problems tracing these faint spiral arms due to their lower amplitude. This is in particular the case for model md0.1mb1, for which the amplitude becomes comparable to the particle noise (see Table 3): it is therefore difficult to unambiguously detect spiral arms.

In Fig. 4 we demonstrate how the number of spiral arms changes with galactic radius. The number of spiral arms and the mass fraction of the disk are measured at $2.2R_{\rm d}$. The relation between the measured number of spiral arms (m) at $2.2R_{\rm d}$ and the disk mass fraction ($f_{\rm d}$) is presented in Fig. 5 where ($f_{\rm d}$) is defined as:

$$f_{\rm d} \equiv \left(\frac{V_{\rm c,d}(R)}{V_{\rm c,tot}(R)} \right)^2_{R=2.2R_{\rm d}}, \qquad (11)$$

where $V_{\rm c,d}$ and $V_{\rm c,tot}$ are the circular velocity of the disk and of the whole galaxy, respectively. We find that m, before the bar formation, decreases as $f_{\rm d}$ increases. This matches the results of D'Onghia (2015) (their figure 3).

The number of spiral arms is furthermore expected to depend on the shear rate:

$$\Gamma = -\frac{d\ln\Omega}{d\ln R}, \qquad (12)$$

where Ω is the angular velocity. The value of Γ indicates the shape of the rotation curve: $\Gamma = 1$ indicates a flat rotation curve, $\Gamma > 1$ indicates a declining rotation curve, and $\Gamma < 1$ indicates an increasing rotation curve. Athanassoula (1984) found that the swing amplification factor also depends on Γ. They computed the swing amplification factor as a function of X for different Γ values and found that the peak amplification factor depends on Γ; $X \sim 1$ for $\Gamma = 0.5$ and $X \sim 2$ for $\Gamma = 1.5$ (see their figure 26). Applying these results to Eq. (9), a smaller value of m is expected for a larger Γ. In Fig. 5, we show the relation between Γ, disk mass fraction ($f_{\rm d}$) and the number of spiral arms (m). In this figure, we confirm that a larger shear rate results in a smaller number of spirals.
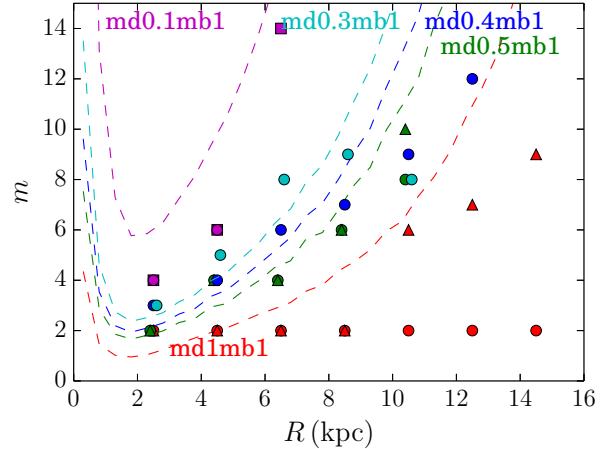
Figure 4. Theoretically predicted (using Eq. 9, dashed curves) and measured number of spiral arms (symbols) for models md0.1mb1 (magenta), md0.3mb1 (cyan), md0.4mb1 (blue), md0.5mb1 (green), and md1mb1 (red) from top to bottom. Filled circles indicate the most frequently appearing number of arms (principal modes) over a 10 Gyr period. Triangle symbols indicates the principal mode before the formation of the bar. Square symbols indicate the principal mode for model md0.1mb1 excluding $m = 2$. The symbols for md0.3mb1 and md0.5mb1 are shifted by 0.1 kpc to avoid overlapping points.
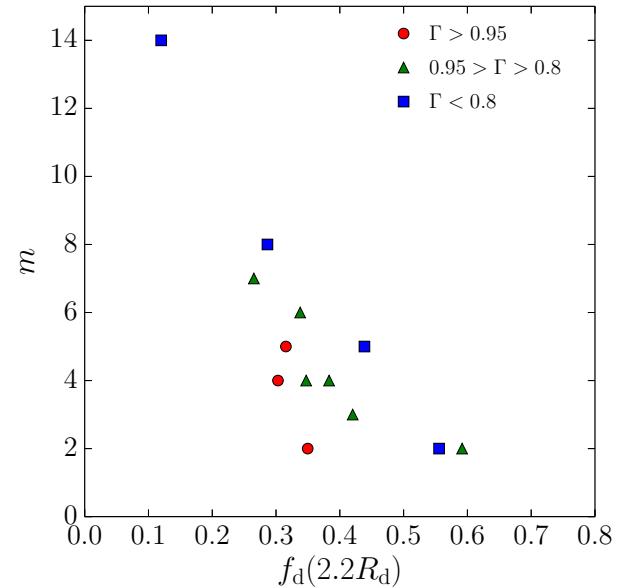

Figure 5. The number of spiral arms (m) before the bar formation epoch. The disk mass fraction ($f_{\rm d} = V_{\rm c,d}(R)^2/V_{\rm c,tot}(R)^2_{R=2.2R_{\rm d}}$) is for the models with $Q_0 = 1.2$ and without halo spin. We measure m at 6.5 kpc, which is close to $2.2R_{\rm d}$, for all models except models md1mb1Rd1.5 and md0.5mb1Rd1.5. For these models $R_{\rm d}$ is 1.5 times larger and we therefore measure m at 9.5 kpc. The shear rate (Γ), measured in the initial conditions at $2.2R_{\rm d}$, is indicated by the different symbols.

Table 3. Pitch angle and number of spiral arms

Model	Radius (R) (kpc)	Shear rate (Γ)	Pitch angle (i) (degree)	Maximum amplitude	Number of arms (m)
md1mb1	10	0.991	18	0.198	2
	12	1.04	18	0.164	2
	14	1.07	19	0.161	2
md1mb1s0.8	8	0.902	18	0.261	2
	10	0.991	19	0.169	2
	12	1.04	18	0.181	2
	14	1.07	22	0.197	2
md0.5mb1	6	0.804	25	0.101	4
	8	0.875	25	0.121	6
	10	0.944	27	0.0836	7
	12	0.983	18	0.0561	2
md0.4mb1	4	0.758	33	0.0372	5
	6	0.796	33	0.0442	6
	8	0.863	27	0.0378	7
	10	0.926	26	0.0249	9
md0.3mb1	4	0.774	32	0.0483	4
	6	0.792	34	0.0453	7
	8	0.847	26	0.0347	9
	10	0.907	29	0.0189	10
md0.1mb1	6	0.744	5	0.00965	1
	8	0.777	3	0.0116	1
	10	0.832	3	0.0111	2
	12	0.885	3	0.0107	2
md0.5mb0	8	0.833	15	0.185	2
	10	0.888	11	0.169	2
	12	0.905	12	0.199	2
md0.5mb3	6	0.991	25	0.131	2
	8	0.955	25	0.119	5
	10	0.963	22	0.0959	3
md0.5mb4	6	0.975	25	0.111	4
	8	0.977	23	0.109	4
	10	0.996	25	1.064	8
md0.5mb4rb3	6	0.963	26	0.0924	5
	8	0.961	25	0.0923	5
	10	0.965	26	0.0725	5
md1.5mb5	8	1.01	21	0.281	2
	10	1.07	16	0.189	2
	12	1.09	14	0.212	2
	14	1.13	11	0.269	2
md1mb10	6	1.10	27	0.287	2
	8	1.07	22	0.269	2
	10	1.05	18	0.211	2
md1mb1Rd1.5	10	0.878	24	0.152	4
	12	0.963	28	0.169	4
	14	1.03	18	0.181	4
md0.5mb1Rd1.5	10	0.850	29	0.0777	7
	12	0.921	27	0.0671	8
	14	0.977	24	0.0572	8
md0.5mb1Rd1.5s	10	0.850	26	0.0719	7
	12	0.921	26	0.0804	7
	14	0.977	24	0.0553	8

3.2.2 Pitch angle

The pitch angle is an important parameter in the discussion on the morphology of spiral galaxies. We measure the pitch angle of our simulated galaxies using the Fourier transform method (see Grand et al. 2013; Baba 2015). Using the same Fourier decomposition (Eq. 10) as for the bar amplitude we compute the phase angle, $\phi_m(R)$. Next, the pitch angle at R

for m is obtained by using

$$\cot i_m(R) = R \frac{d\phi(R)_m}{dR}. \tag{13}$$

In numerical simulations the pitch angle changes over time (Baba et al. 2013; Grand et al. 2013; Baba 2015). The pitch angle of spiral arms increases and decreases repeatedly as the amplitude of transient spiral arms increases

and decreases (see Figures 4 and 5 in Baba 2015). Furthermore, the number of spiral arms also changes as a function of R as we saw in previous sections. We therefore measure the most appearing pitch angle for the most appearing mode (principal mode) at each galactic radius. Following Baba (2015), we define the most frequently appearing pitch angle weighted by the Fourier amplitude as the pitch angle. In Table 3, we report the measured pitch angle and the number of spiral arms (m) for that angle. Note that we measure pitch angles at $\gtrsim 2.2R_d$, except for barred galaxies where we, to avoid the bar's influence, use an R that is larger than the maximum bar length.

Julian & Toomre (1966) suggested that the pitch angle (i) is determined by the shear rate (Γ, see Eq. 12 and Table 3) of the disk. The relation between the shear rate and pitch angle was recently investigated using both numerical simulations and analytic models (Michikoshi & Kokubo 2014, 2016a). The relation is also suggested by galaxy observations (Seigar 2005; Seigar et al. 2006). In Fig. 6, the relation between Γ and i is presented (averaged for each model). In order to compare our results with the theory, we also present the relation between Γ and i as derived by (Michikoshi & Kokubo 2014):

$$\tan i = \frac{7}{2} \frac{\sqrt{4-2\Gamma}}{\Gamma}. \tag{14}$$

In the figure this relation is presented with a dashed curve. Except for models md0.5mb0 and md0.1mb1, the measured relation in our simulations is consistent with the theoretical curve.

We now briefly discuss these two outliers. Model md0.5mb0 has, due to the lack of a bulge component, a strong bar resulting in a ring structure around the bar end (see Fig. 3). Here the ring structure may affect the spiral structure in the outer disk region. The pitch angle as measured before bar formation ($t < 2.5$ Gyr) is 23° and m =5–10 at $R = 8$–12 kpc which is consistent with the curve in Fig. 6.

The other outlier, md0.1mb1, has a relatively low-mass disk which results in low-contrast spiral structure (virtually invisible; see Fig. 3). The amplitude, ~ 0.01 (see Table 3), is comparable to the particle noise level (see Fig. 7). This makes it difficult to accurately measure the number of spiral arms and their pitch angle using the scheme we adopted.

We also present the relation between the shear rate and the pitch angles of observed galaxies (Seigar et al. 2006) in Fig. 6 (black points). These points are also distributed around the theoretical curve with a scatter larger than the simulated galaxies.

3.3 Bar Formation

We will now investigate the formation of bars. In order to define the bar formation, we measure the time evolution of the length (radius) of the bar and its amplitude which develops in our galaxy simulations. Because this has to be done for one thousand snapshots for each galaxy simulation we adopt a relatively simple method for measuring these properties. We measure the Fourier amplitude (Eq. 10) in radial bins of 1 kpc for the $m = 2$ mode ($A_2(R)$), record the maximum value and use this as the bar amplitude ($A_{2,\max}$). In the left panel of Fig. 7, we present the time evolution of
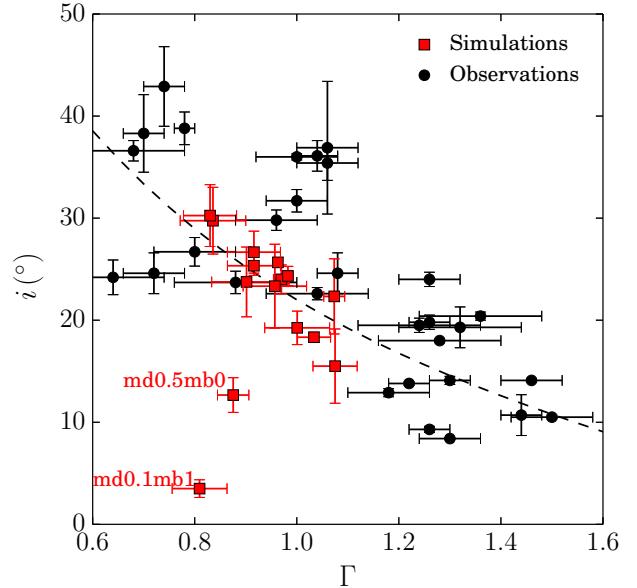

Figure 6. The relation between shear rate (Γ) and pitch angle (i) for the simulated galaxies shown in Table 3 (red squares) and observed galaxies (Seigar et al. 2006) (black circles). For simulated galaxies, the error bars on the x-axis indicate the range of shear rates depending on the radius at which we measured Γ and i. The error bars on the y-axis indicate the standard deviations of the measured pitch angles at each radius. The black dashed curve indicates the result of Michikoshi & Kokubo (2014) given by equation (14).

$A_{2,\max}$ for models md1mb1 to md0.1mb1. Once a bar begins to develop the amplitude increases exponentially and either reaches a stable maximum (as is the case in model md1mb1) or decreases slightly to increase again a few Gyr later (see model mb0.5mb1). Model md0.1mb1 did not form a bar within 10 Gyr.

We also measure the bar length using the method described in Scannapieco & Athanassoula (2012) and Okamoto et al. (2015). In this method we compute the phase angle ($\phi_2(R)$) and amplitude ($A_2(R)$) of the bar at each radius using the Fourier analysis (Eq. 10). As R increases, $A_2(R)$ increases, reaches its maximum in the middle of the bar, and then decreases. We define the radius at which $A_2(R)$ reaches its maximum value as $R_{\max}$ and the phase at $R_{\max}$ as the phase angle of the bar ($\phi_{2,\max}$). Starting at $R_{\max}$, we compare $\phi_2(R)$ with $\phi_{2,\max}$. When $\Delta\phi = |\phi_2(R) - \phi_{2,\max}| > 0.05\pi$, we consider that the bar has ended and define the radius as the bar's size, R_b. Hereafter, we refer to R_b as the length of the bar. The time evolution of the bar length is presented in the right panel of Fig. 7. The length of the bar grows continuously until the end of simulation ($t = 15$ Gyr).

We define the epoch of bar formation (t_b) as the moment when $A_{2,\max} > 0.2$ and $R_b > 1$ kpc. In our models the bar was always longer than 1 kpc when $A_{2,\max} > 0.2$. In most cases the bar amplitude increases exponentially and therefore the critical amplitude has little effect on the moment the bar forms. For models md0.4mb1 and md0.3mb1, which did not form a bar within 10 Gyr, we continued the simulations until

a bar formed after 13 and 18 Gyr, respectively (also see Fig. 7 and Table 4). We continued the simulations up to 15 Gyr for md0.5mb4 and md0.5mb4rb3 to confirm that they form a bar, which they do around ~ 10 Gyr.

We subsequently investigate the effect of the bulge mass on the bar formation. It was suggested that a massive central component, such as a bulge, have a stabilizing effect on the disk and thereby prevents bar formation (Sellwood & Evans 2001; Saha & Naab 2013). To test this we perform a set of simulations in which we vary the bulge mass. We make the bulge 0 (md0.5mb0), 3 (md0.5mb3) and 4 (mb0.5mb4) times as massive as the bulge of model md0.5mb1. We further added model md0.5mb4rb3 with the same mass as md0.5mb4, but with increased bulge scale length. The amplitude evolution and bar length of these models is presented in Fig. 8. When the bulge mass fraction increases the bar formation is delayed due to the the decreasing disk mass-fraction ($f_{\rm d}$) (also see Table 4). These results are consistent with observations where the fraction of barred galaxies increase when the bulge to disk mass ratio decreases and where the barred galaxies fraction even increases to $\sim 87\%$ for the extreme case of bulge-less galaxies. We further confirm that the bulge scale length does not effect the epoch of bar formation, but the bar length at the end of the simulation (at 15 Gyr). The final bar length for model md0.4mb4rb3 is longer than that for md0.4mb4 (see Fig. 8). The bar formation epoch for all models is presented in Table 4.

Although increasing the bulge mass sequentially delays the formation of a bar, the bulge mass fraction is not a critical parameter for the bar formation. We tested some parameters and found that the disk-mass to the total mass fraction is a more critical parameter for the bar formation epoch.

In Fig. 9, we present the relation between the bar formation epoch and the disk mass fraction, $f_{\rm d}(= 1/X')$, where X' is a parameter adopted by Widrow et al. (2008) as a bar formation criterion:

$$X' \equiv 1/f_{\rm d} = \left(\frac{V_{\rm c,tot}(R)}{V_{\rm c,d}(R)} \right)^2_{R=2.2R_{\rm d}} . \tag{15}$$

They argued that $X' \lesssim 3$ (for $f_{\rm d} \gtrsim 0.3$) is the bar formation criterion in their simulation. The epoch of bar formation increases exponentially for decreasing disk mass-fraction, although the scatter is large. We fit an exponential function to our results obtained with $N_{\rm d} = 8$M and $Q_0 = 1.2$ and find that $t_{\rm b} = 0.146 \pm 0.079 \exp[(1.38 \pm 0.17)/f_{\rm d}]$. The result is indicated by the dashed black line in Fig. 9.

The resolution of the simulation in the number of particles is an important source for the scatter (Dubinski et al. 2009); a smaller number of particles for the same model results in faster bar formation. We confirm this by performing simulations with an order of magnitude lower resolution (0.8 M disk particles, open circle symbols), and indeed find that the bar forms earlier for these models in comparison with the high resolution models (Fig. 9, Table 4). Another parameter which is known to affect the epoch of bar formation is the value of Q. In Fig. 9 we also plot models md0.5mb1Q2.0 and md0.5mb1Q0.5, which are identical to model md0.5mb1, with the exception that $Q_0 = 2.0$ and 0.5, respectively. As was shown in previous studies (c.f., Athanassoula & Sellwood 1986), a larger value of Q_0 leads to a delay in the formation of the bar (see Appendix A2 for details).

The relation between the moment of bar formation ($t_{\rm b}$) and the mass fraction of the disk ($f_{\rm d}$) can be understood from Toomre's X parameter (see Eq. 6). For a given value of m we can calculate X as a function of the disk radius R. When we adopt $m = 2$, i.e. the bar, we obtain X for the bar mode (X_2) as a function of R. This distribution is presented in Fig. 10. Here, we see that X_2 reaches minimum values at $R \sim 2$ kpc. We find that the minimum value of X_2 ($X_{\rm min}$) is roughly correlated with $X'(= 1/f_{\rm d})$, and the relation between $X_{\rm min}$ and X' is presented in Fig. 11. Thus, the disk fraction $f_{\rm d}$ is connected to Toomre's X. As shown by Toomre (1981), the amplitude grows most efficiently for $1 < X < 2$ and decreases exponentially when X increases from ~ 2 to ~ 3. We find that models in which a bar forms have a minimum value of $X_2 \lesssim 2$ (see Fig. 10). We conclude, based on these results, that there is no particular rigid criterion for bar formation, but that the bar formation epoch starts to increase exponentially when $f_{\rm d} \gtrsim 0.3$, or equivalently, if $X' \lesssim 0.3$.

We also test the bar formation criterion previously suggested by Efstathiou et al. (1982), who proposed that bar formation depends on the mass of the disk ($M_{\rm d}$) within radius $R_{\rm d}$:

$$\varepsilon_{\rm m} \equiv \frac{V_{\rm c,max}}{(GM_{\rm d}/R_{\rm d})^{1/2}} < 1.1. \tag{16}$$

Here $V_{\rm c,max}$ is the maximum circular velocity in the disk. For this criterion, Athanassoula (2008) showed some exceptional cases using N-body simulations of disk models with live halos. In Table 4, we present $\varepsilon_{\rm m}$ (Eq. 16), and we confirm that in our simulations Efstathiou's criterion cannot always predict the bar formation.

3.4 Bulge-to-Disk mass ratio

From an observational perspective such as in the Hubble sequence (Hubble 1926), the bulge-to-disk mass ratio (B/D) is related to the pitch angle. Sa galaxies have a larger bulge-to-disk mass-ratio compared to Sb and Sc galaxies (Sandage 1961). To test this hypothesis, we simulate an extra model (md1mb10), with a much larger B/D than the the other models.

The disk-to-halo mass ratio of this model is relatively large ($B/D = 1.0$), but the disk-to-total mass ratio ($f_{\rm d} = 0.35$) is not as large as for models which form a bar before forming spiral arms. The S0–Sa galaxies, for example, NGC 1167 (Zasov et al. 2008) and M 104 (Tempel & Tenjes 2006), have such a massive bulge and also many narrow spiral arms.

In Fig. 12 we present the rotation curves (left panel) and the surface-density images (middle and right panels) for model md1mb10. This model formed multiple spiral arms similar to Sa galaxies before it developed a bar. The measured pitch angle was $\sim 20°$ within 10 kpc but less than $10°$ at $R > 10$ kpc.

In the previous subsection, we demonstrated the relation between the pitch angle and the shear rate (Γ). Here, in Fig. 13, we present the relation between Γ and the bulge-to-disk mass ratio (B/D). For our models with $f_{\rm d} > 0.3$, Γ appears to correlate with B/D, however the models with a small $f_{\rm d}$ tend to have a small Γ. In the latter sequence, the bulge mass is similar but the disk mass decreases as B/D increases and as a result $f_{\rm d}$ decreases.

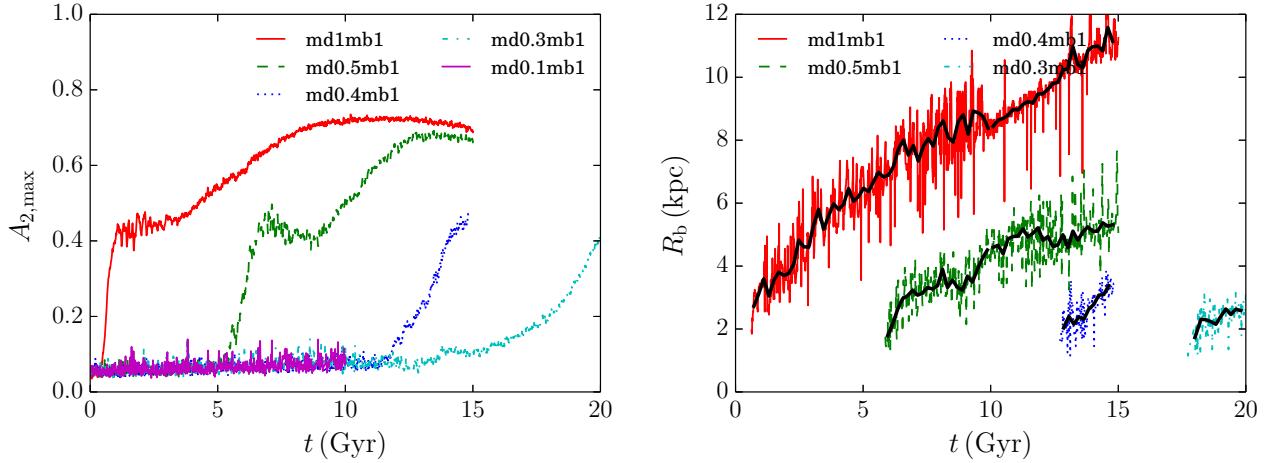In order to understand how the initial parameters affect

Figure 7. Time evolution of the maximum amplitude for $m = 2$ (left) and the bar length (right) for models md0.1mb1, md0.3mb1, md0.4mb1, md0.5mb1, and md1mb1.. Black curves in the right panel indicate the bar length averaged over every 20 snapshots (~ 0.2Gyr).
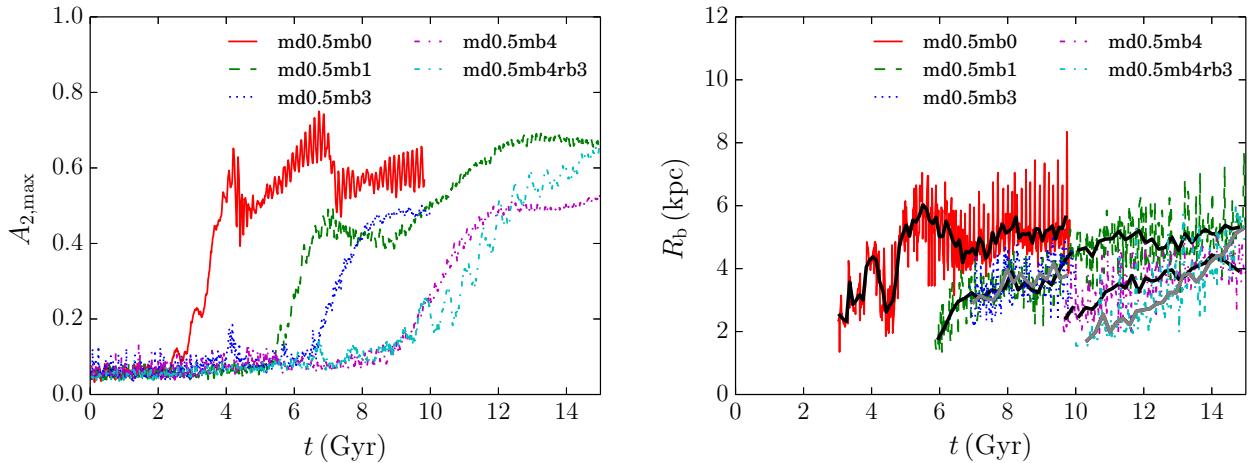

Figure 8. Same as Fig. 7 but for models md0.5mb0, md0.5mb1, md0.5mb3, md0.5mb4, and md0.5mb4rb3.

the combination of B/D and Γ, we create an additional set of models. Here we measure the properties in the initial realizations without actually running the simulations. When we keep the disk mass fraction ($f_{\rm d}$) and the bulge scale-length ($r_{\rm b}$) fixed then Γ increases as B/D increases. Even when we compare models that have similar B/D and $f_{\rm d}$, we find that models with a larger $r_{\rm b}$ have a larger Γ. And when we increase $f_{\rm d}$, while keeping B/D fixed, then Γ increases. We also tested the effect of the halo scale length parameter but found that this did not affect B/D or Γ substantially. These sequential changes in the relation between B/D and Γ are summarized in Fig. C1 of Appendix C, and the detailed parameters of the individual models are summarized in Tables C1 and C2. Thus, galaxies with a massive bulge tend to form tightly-wound spirals, but the shear rate (Γ) is more essential to the pitch angle than B/D.

In addition, we look at the relation between B/D and the bar formation epoch ($t_{\rm b}$). We present this using the red symbols for models with $B/D > 0.5$ in Fig. 9. Models with a large B/D tend to take a shorter time before the bar for-

mation, but compared to the dependence on $f_{\rm d}$, the effect of B/D on $t_{\rm b}$ is unclear.

Summarizing all our simulated results, we conclude that the disk-to-total mass fraction ($f_{\rm d}$) and the shear rate (Γ) are important parameters that decide the disk galaxy morphology, such as the number of spiral arms, the pitch angle, and the formation of a bar.

4 DISCUSSIONS

4.1 Hubble sequence and galaxy morphology

We performed N-body simulations of disk galaxies which start in an axisymmetric equilibrium state and which form spiral and bar structures. Using these simulations we investigated the relation between changes in the initial state of the bulge, disk, and halo (initial conditions in the simulations) and the resulting morphology of the disk galaxies.

Especially the disk-mass fraction ($f_{\rm d}$) and shear rate (Γ) are important parameters which influence the morphology of the simulated galaxies. While $f_{\rm d}$ determines the number of

Table 4. Details on the formation of the bar. The columns give the model name, a boolean indicating if a bar formed (Y) or not (N) within the simulation time period (0–20 Gyr), the moment and criteria of the bar formation.

Model	Bar formation	Bar formation epoch t_b (Gyr)	Bar formation criteria ε_m	X_{min}	$X'(\equiv 1/f_d)$
md1mb1	Y	0.64	0.824	0.997	1.80
md1mb1s0.65	Y	0.83	0.824	0.997	1.80
md1mb1s0.8	Y	0.73	0.824	0.997	1.80
md0.5mb1	Y	6.3	1.03	1.68	2.61
md0.4mb1	Y	13	1.00	1.97	2.96
md0.3mb1	Y	18	1.87	2.41	3.49
md0.1mb1	N	-	2.12	5.78	8.34
md0.5mb0	Y	3.1	1.08	0.827	2.28
md0.5mb3	Y	7.0	1.26	2.17	2.88
md0.5mb4	Y	9.9	1.38	2.58	3.06
md0.5mb4rb3	Y	9.9	1.15	2.80	3.17
md1.5mb5	Y	1.9	1.42	1.30	1.69
md1mb10	Y	7.5	1.60	2.71	2.86
md1mb1Rd1.5	Y	2.6	0.960	1.41	2.38
md0.5mb1Rd1.5	N	-	1.25	2.35	3.77
md0.5mb1Rd1.5s	N	-	1.25	2.35	3.77
md0.5mb1Q0.5	Y	0.27	1.03	1.68	2.61
md0.5mb1Q2	Y	8.8	1.03	1.68	2.61
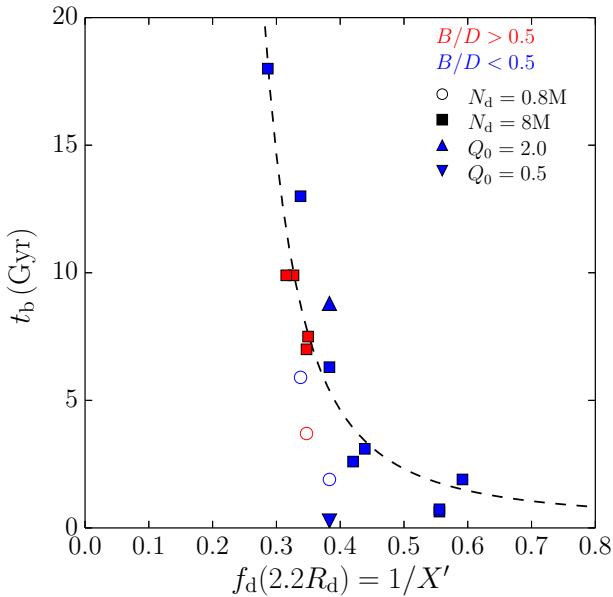
Figure 9. Bar formation epoch (t_b) and disk mass fraction ($f_d = 1/X'$). Filled squares and open circles indicate models with $N_d = 8M$ and $0.8M$, respectively. Red (blue) indicates models with a bulge-to-disk mass ratio (B/D) of > 0.5 (< 0.5). The dashed curve indicates a fit to the models with $N_d = 8M$ and $Q_0 = 1.2$ (squares): $t_b = 0.146 \pm 0.079 \exp[(1.38 \pm 0.17)/f_d]$.
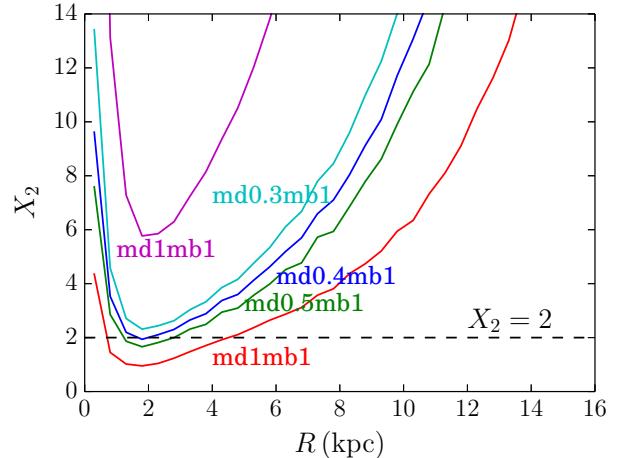
Figure 10. X values as a function of radius for $m = 2$ mode.

spiral arms and the bar formation epoch, Γ has some influence on the bar formation epoch and more strongly affects the spiral arms pitch angle.

Observationally, disk galaxies are classified using the Hubble sequence (Hubble 1926). In the Hubble sequence, spiral galaxies are classified either as spirals (SA) or barred spirals (SB). Each of these two branches has sub-types a to d; where the bulge-to-disk mass ratio (B/D) decreases and the pitch angle increases as we go from a to d (Sandage 1961). In this section, we discuss how the Hubble sequence can be understood by the disk's initial configuration and secular evolution.
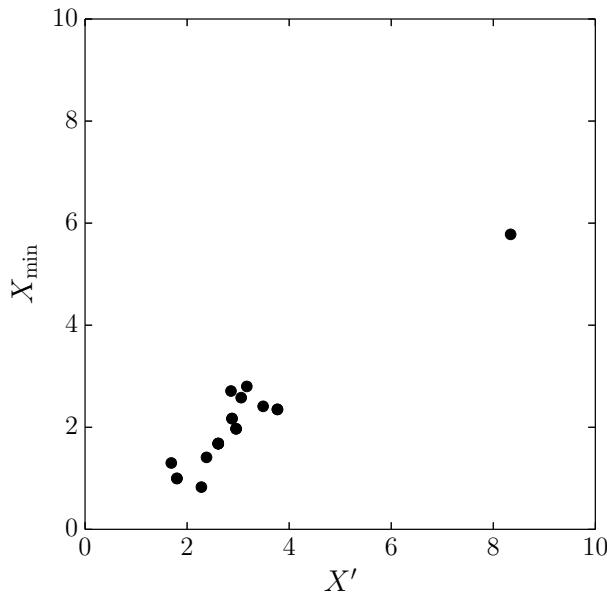
Figure 11. Relation between X' and the minimum value of X (X_{min}).

In Fig. 14 we present a subset of snapshots from our simulation on the Hubble sequence. In the Hubble sequence, the spirals are more loosely wound and the bulge becomes fainter when moving from Sa to Sc. This is connected with the results we see in Section 3 where galaxies with a massive bulge have more tightly wound spiral arms due to the larger shear rate when the disk mass fraction is kept similar. Indeed, selecting some models, we see that the sequence of spiral galaxies from Sa to Sc originates from changes in the initial distribution of the disk, bulge and dark matter halo. However, B/D does not linearly change the shear rate (Γ) as we demonstrated in Section 3.4 (see also Appendix C). The shear rate also increases with the disk mass fraction (f_d). Therefore, Γ is a more direct parameter to influence the pitch angle rather than B/D. Of course galaxies with a massive bulge tend to have tightly winding spirals because they tend to have a larger Γ.

Flocculent galaxies emerge from models with a small disk to total-mass fraction (such as in model md0.1mb1). Even after 10 Gyr this model did not form a bar and the data in Fig. 9 indicates that it will take more than a Hubble time before the bar forms.

Once the bar formation criteria is satisfied the spiral galaxies leave the spiral sequence and move into the SB sequence. If the barred galaxy started as a Sc galaxy then in the early stages it resembles the barred-spiral structures as seen in SBc galaxies. These galaxies continue to evolve towards SBb galaxies. For example, model md0.5mb0 has a strong bar and the spirals become more tightly wound in the later phases (see Figs. 2 and 3).

The de Vaucouleurs classification (de Vaucouleurs 1959) appears when spiral galaxies evolve into barred galaxies. In the models where the disk is massive enough to form a bar, but less massive than the models md0.5mb1 and md1mb1Rd1.5, a ring structure just outside of the bar ap-

pears after the bar has formed. In Fig. 3 and A9 we see that these models still retain some spiral structures in the outer parts of the disks. For models md1mb1 and md1.5mb5, which have a disk mass with $f_d > 0.5$, a bar forms directly after the start of the simulations (see Fig. 9). They further form strong s-shaped and outer ring structures after the bar fully developed (right most of Fig. 3). For these models we do not observe any clear spiral structure in the outer regions of the disk. This may be due to the absence of gas in our simulations (Bottema 2003).

Although we did not take gas into account in our simulations, the fraction of gas is an important factor for the morphology of disk galaxies. Shlosman & Noguchi (1993) suggested that bar formation is prevented if more than 10% of the disk's mass is in the form of gas. Bottema (2003) also performed a series of simulations that included gas and concluded that the bar stability depends on the presence of gas. We ignore the formation of disks that start from gas rich models. Such disk galaxies have been observed at a redshift of ~ 1 (Genzel et al. 2017). The effects of gas, however, must be considered in order to fully understand the morphology of disk galaxies. In addition, the galaxies in our study are not positioned in a cosmological framework, which would be necessary to also take the merging history of disk galaxies into account. However, disk galaxies seem to be formed with a relatively quiet merging history (e. g., Steinmetz & Navarro 2002; Abadi et al. 2003). Therefore, our study could be a testbed for studying the origin of disk galaxy morphology.

4.2 Non-barred grand-design spirals

As described in Section 3.3, swing amplification theory predicts that galaxies with massive disks (large disk-to-halo mass fraction) typically develop two spiral arms. This condition at the same time satisfies the constraints for the rapid formation of a bar. Both two-armed spirals and bars are structures of $m = 2$. In our models, galaxies with a massive disk often directly form a bar rather than first forming a two-armed spiral disk. This implies that $m = 2$ structures in galactic disks are mostly bars. However, from observations we know that non-barred grand-design spiral galaxies do actually exist. One possible cause is that perturbations induced by a companion galaxy leads to the formation of such a spiral galaxy. This was tested by Toomre & Toomre (1972) who, using simulations, showed that tidal interactions can lead to the formation of two spiral arms without a bar. Recently, Pettitt & Wadsley (2018) also showed this using simulations that included gas. If accompanying galaxies are indeed the driver for the formation of two armed spirals then the number of grand-design spirals with companions must exceed the number of isolated grand-design galaxies. Kormendy & Norman (1979) and Elmegreen & Elmegreen (1982) observationally showed that disk galaxies with companions consist of a larger fraction of grand-design spirals (0.6–1.0) compared to isolated galaxies (0.2–0.3). However, not all non-barred grand-design spiral galaxies have companions. M 74, for example, has no apparent companion (Kendall et al. 2011). In the following paragraphs we explore the formation of non-barred grand-design spirals without a companion.

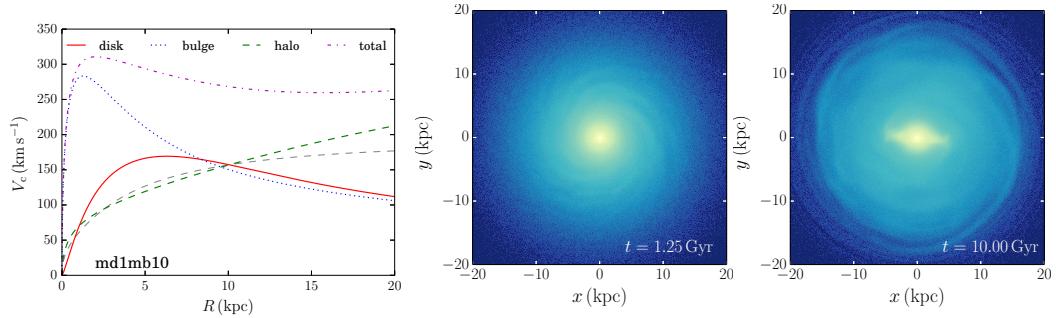In the previous sections we saw that a massive disk leads

Figure 12. Rotation curve (left) and surface density at 1.25 Gyr (middle) and 10 Gyr for model md1mb10. Gray dashed curve in the left panel indicates the rotation curve of the halo for model md1mb1.
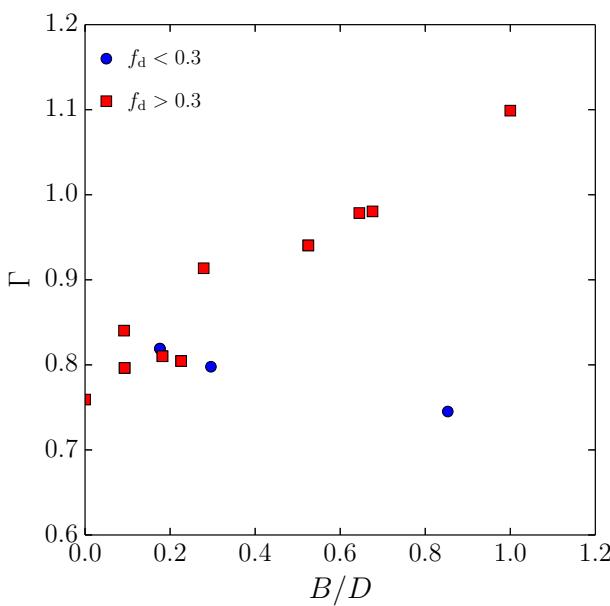

Figure 13. The relation between the shear rates at $2.2R_d$ and the bulge-to-disk mass ratio of our models. Circles and squares indicate models with $f_d(2.2R_d) < 0.3$ and $f_d(2.2R_d) > 0.3$, respectively.

to $m = 2$ structures. On the other hand, a massive bulge suppresses the formation of a bar, but massive bulges tend to increase the number of spiral arms (e.g. model md1mb10). To create a non-barred grand-design spiral we therefore setup a new model, md1.5mb5, which has the largest disk mass-fraction of all our models ($f_d \sim 0.6$), and a moderately massive bulge, $B/D \sim 0.3$. This model is expected to form a bar. In Fig. 15 we present the initial rotation curve (left panel) and the density snapshots (right panels) for this model. At an age of $t = 1.25$ Gyr this model shows structure comparable to that observed in non-barred grand-design spirals, but only in the short time before the bar is formed. We conclude that non-barred grand-design spirals can form without companion, but that the structure is short-lived and disappears as soon as the bar forms. In our simulations we ignore the presence of gas, which may change the results. Bottema (2003), however, performed a series of simulations that included gas dynamics, and they also concluded that a companion is nec-

essary for non-barred grand-design spirals (see also a review by Dobbs & Baba 2014).

5   SUMMARY

We performed a series of galactic disk N-body simulations to investigate the formation and dynamical evolution of spiral arm and bar structures in stellar disks which are embedded in live dark matter halos. We adopted a range of initial conditions where the models have similar halo rotation curves, but different masses for the disk and bulge components, scale lengths, initial Q values, and halo spin parameters. The results indicate that the bar formation epoch increases exponentially as a function of the disk mass fraction with respect to the total mass at the reference radius (2.2 times the disk scale length), f_d. This relation is a consequence of swing amplification (Toomre 1981), which describes the amplification rate of the spiral arm when it transitions from leading arm to trailing arm because of the disk's differential rotation. Swing amplification depends on the properties that characterize the disk, Toomre's Q, X, and Γ. The growth rate reaches its maximum for $1 < X < 2$, although the position of the peak slightly depends on Q as well as on Γ. We computed X for $m = 2$ (X_2), which corresponds to a bar or two-armed spiral, for each of our models and found that this value is related to the bar's formation epoch.

The bar amplitude grows most efficiently when $1 < X_2 < 2$. For models with $1 < X_2 < 2$ the bar develops immediately after the start of the simulation. As X_2 increases beyond $X_2 = 2$, the growth rate decreases exponentially. We find that the bar formation epoch increases exponentially as X_2 increases beyond $X_2 = 2$, in other words f_d decreases. The bar formation epoch exceeds a Hubble time for $f_d \lesssim 0.35$.

Apart from X, the growth rate is also influenced by Q where a larger Q results in a slower growth. This indicates that the bar formation occurs later for larger values of Q. Our simulations confirmed this and showed that for the bar ($m = 2$) the growth rate is predicted by swing amplification and becomes visible when it grows beyond a certain amplitude.

Toomre's swing amplification theory further predicts that the number of spiral arms is related to the mass of the disk, with massive disks having fewer spiral arms. In addition, larger Γ predicts a smaller number of spiral arms. We confirmed these relations in our simulations. The shear rate (Γ) also affects the pitch angle of spiral arms. We fur-
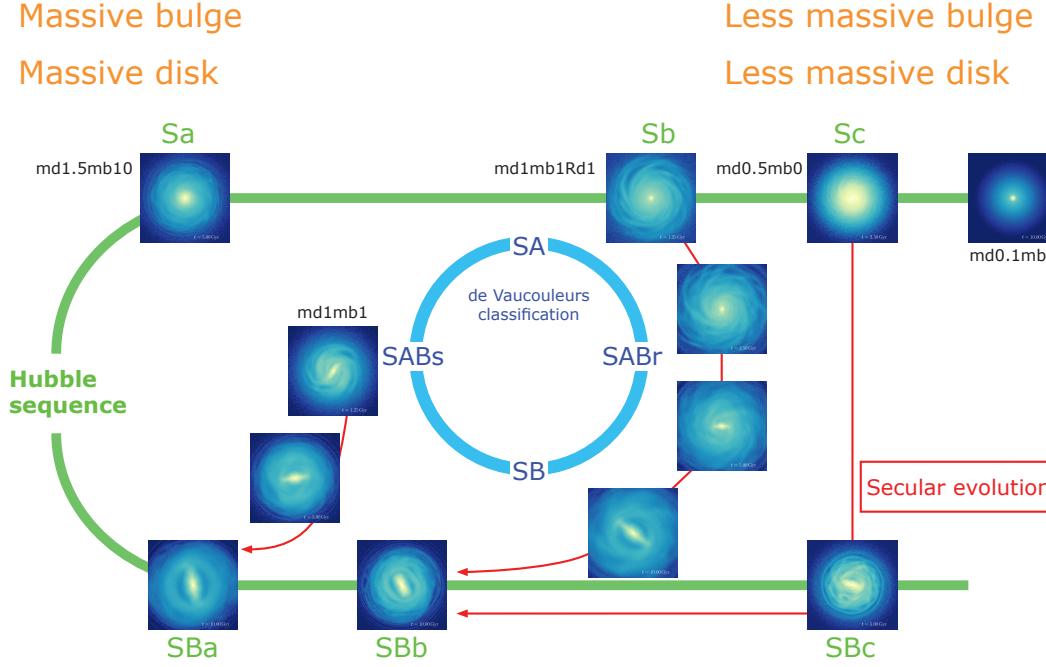
Figure 14. The Hubble sequence and de Vaucouleurs classification overlaid with snapshots of our models. The red arrows show the models secular evolution.
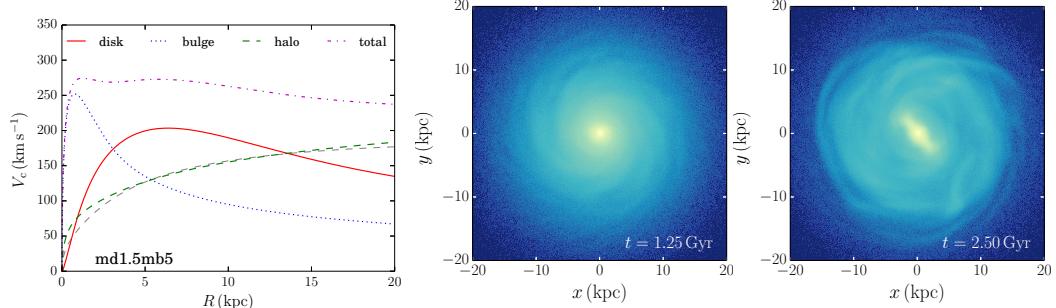

Figure 15. Initial rotation curves (left) and density snapshots for model md1.5mb5 at $t = 1.25$ Gyr (middle) and $t = 2.5$ Gyr (right). The gray dashed curve in the left panel is the same as the one in Fig. 12.

ther confirmed that our result is consistent with previous studies.

We found that the disk-to-total mass fraction (f_d) and the shear rate (Γ) are the most important parameters that determine the morphology of disk galaxies. When juxtaposing our models with the Hubble sequence, the fundamental subdivisions of (barred-)spiral galaxies with massive bulges and tightly wound-up spiral arms from S(B)a to S(B)c is also be observed as a sequence in our simulations. Where the models with either massive bulges or massive disks have more tightly wound spiral arms. This is because having both a massive disk and bulge results in a larger Γ, i.e., more tightly wound spiral arms.

Once the bar is formed it starts to heat the outer parts of the disk. From this point onwards, the self-gravitating spiral arms disappear. This may be in part caused by the lack of gas in our simulations. After the bar grows, we no longer discern spiral arms in the outer regions of the disk. This could imply that gas cooling and star formation are required in order to maintain spiral structures in barred spiral galaxies for over a Hubble time (Schwarz 1981; Sellwood & Carlberg 1984).

Our simulations further indicate that non-barred grand-design spirals are transient structures which immediately evolve into barred galaxies. Swing amplification teaches us that a massive disk is required to form two-armed spiral galaxies. This condition, at the same time, satisfies the short formation time of the bar structure. Non-barred grand-design spiral galaxies therefore must evolve into barred galaxies. We consider that isolated non-barred grand-design spiral galaxies are in the process of developing a bar.

APPENDIX A: THE EFFECTS OF OTHER PARAMETERS

We discussed the effect of the bulge and disk masses on the development of bars and spiral arms in the main text. Here we briefly summarize the effects of the other parameters we investigated.

A1   The halo spin

The spin of the halo is known to be an important parameter that affects the bar's secular evolution. Long et al. (2014) showed that a co-rotating disk and halo speed up the bar formation, but decrease its final length. This is due to the angular momentum transfer between the disk and halo. If the halo does not spin it absorbs the bar's angular momentum, which slows down the bar and increases its length. A co-rotating halo, however, returns angular momentum to the disk instead of just absorbing it. This stabilizes the angular momentum transfer, and the bar evolution ceases.

We setup a few models, based on model md1mb1, but now with a rotating halo. In order to give spin to the halo we change the sign of the angular momentum z component, L_z. For models md1mb1s0.65 and md1mb1s0.8, 65 and 85 % of the halo particles are rotating in the same direction as the disk. For models without rotation, this value is 50 %.

To compare our results with previous studies, we measure the spin parameter Peebles (1969, 1971):

$$\lambda = \frac{J|E|^{1/2}}{GM_{\mathrm{h}}^{5/2}}, \tag{A1}$$

where J is the magnitude of the angular momentum vector, and E is the total energy. In our models, $\alpha_{\mathrm{h}} = 0.65$ (0.8) correspond to $\lambda \sim 0.03$ (0.06).

In Fig. A1 we present the effect that the halo spin has on models md1mb1s0.65 and md1mb1s0.8. The results indicate that the bar is shorter for the models with a stronger halo spin.

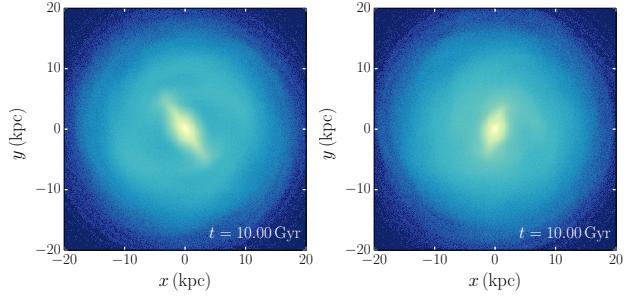In Fig. A2 we show the length and maximum amplitude

Figure A1. Snapshots for models md1mb1s0.65 (left) and md1mb1s0.8 (right), which are the same as model md1mb1 (Fig. 3,far most right panel) but now including halo spin.

of the resulting bars. These results are consistent with previous results which show that the length of the bar and its amplitude decay when the halo spin increases. However, in contrast to Saha & Naab (2013) and Long et al. (2014) , we find that the epoch of bar formation in our models is similar, whereas a faster formation was expected based on the larger halo spin. In order to rule out the effect of run-to-run variations (Sellwood & Debattista 2009), we performed four additional simulations for each of models md1mb1, md1mb1s0.65 and md1mb1s0.8. For the bar formation epochs we calculated the average and standard deviation.

The average bar formation-epoch is 0.674 ± 0.053, 0.691 ± 0.083, and 0.610 ± 0.069 Gyr for models md1mb1, md1mb1s0.65 and md1mb1s0.8, respectively. This may be caused by the relatively early bar formation (within $\sim$ 0.8 Gyr) compared to the previous studies; 1–2 Gyr for Long et al. (2014) and 3–4 Gyr for Saha & Naab (2013). Indeed, in Long et al. (2014) the bar formation epoch starts slightly earlier when a moderate spin parameter ($\lambda = 0.045$ and 0.06) is introduced. The dependence of the bar formation-epoch on the halo spin is even clearer in Saha & Naab (2013), where the formation time is longer than in Long et al. (2014). We therefore argue that the rapid bar formation in our models may hide the sequential delay of the bar formation as caused by the halo spin.

In addition to the bar forming models above, we also added halo spin to a model that shows no bar formation within 10 Gyr. This model, md0.5Rd1.5s, is based on md0.5Rd1.5 but now with a halo spin of 0.8. In Fig. A3, we present the snapshots of the above models at $t = 10$ Gyr. In contrast to the barred galaxies, their spiral structures look quite similar. To quantitatively compare the spiral amplitudes we use the total amplitude of the spiral arms given by $\sum_{m=1}^{10} |A_m|^2$, where A_m is the Fourier amplitude (Eq. 10). Instead of the bar amplitude, we measured the spirals total amplitude at $2.2R_{\mathrm{d}}$ and at $4.5R_{\mathrm{d}}$ (for this model 9.5 and 19.5 kpc, respectively), the results are shown in Fig. A4. The evolution of the spiral amplitudes are quite similar for both models, just like the pitch angle $24°$–$29°$ (with) $24°$–$26°$ (without halo spin) and the number of spiral arms $m = 7$–8 for $R = 10$–14 kpc (see Table 3).

In addition, in Fig. A5 we investigate the angular-momentum flow for the disk and halo as a function of time and cylindrical radius. Following Long et al. (2014) and Villa-Vargas et al. (2009), we measure the change in angular momentum of the z-component at every ~ 10 Myr. For the
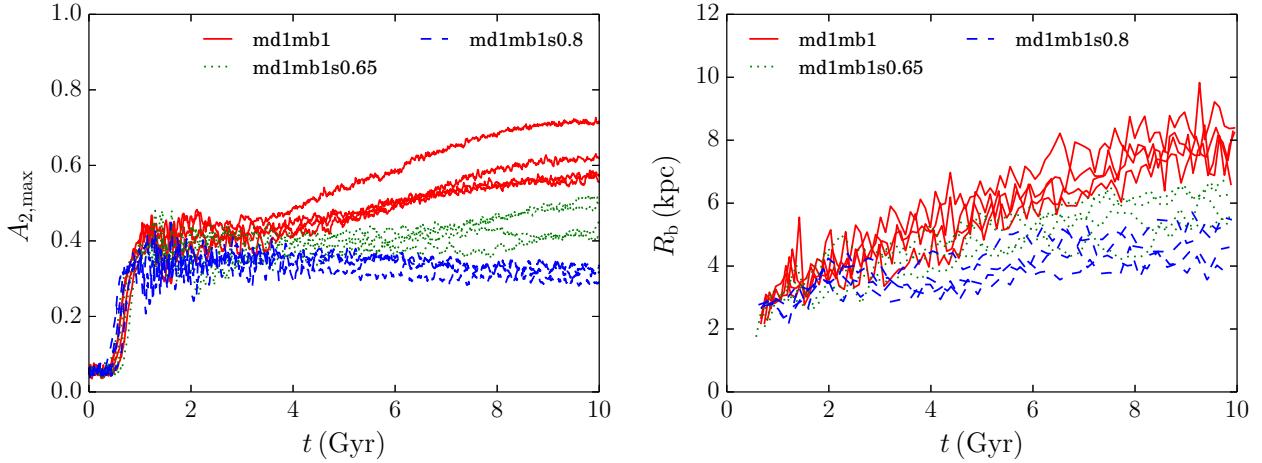
Figure A2. Time evolution of the maximum amplitude for $m = 2$ (left) and the bar length (averaged for every $\sim 0.1\,\mathrm{Gyr}$) for models md1mb1, md1mb1s0.65, and md1mb1s0.8. For each model, we performed four simulations changing the random seed (varying positions and velocities of the particles) when generating the initial realizations.
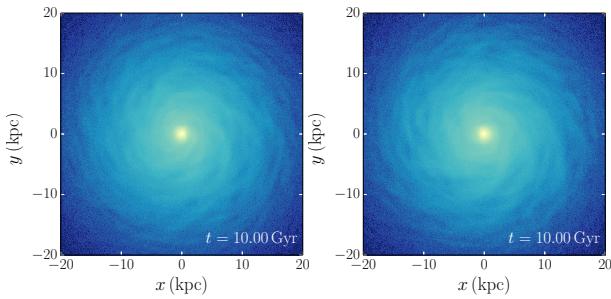

Figure A3. Snapshots for models md0.5Rd1.5 (left) and md0.5Rd1.5s (right).

halos (top panels) there is no continuous angular momentum transfer from the disk to the halo, but we only discern random variations in the angular momentum. These fluctuations look stronger at outer radii, but this is because the angular momentum changes are normalized by the disk' angular momentum, which is smaller in the outer regions.

The angular momentum of the disks vary with time (see the red and blue stripes in the bottom panels), but overall the disk loses only 1.9 % of its initial angular momentum for models with spin and 1.7 % for models without. The amplitude of the stripes for the disks roughly corresponds to the amplitude of the spiral pattern. In Fig. A6, we show the total power as a function of cylindrical radius and time for models md0.5Rd1.5 (left) and md0.5Rd1.5s (right). From this we conclude that for spiral arms the angular momentum transfer between the disk and the halo is not efficient. On the other hand, for barred galaxies the angular momentum flow from the disk to the halo is considerably smaller for models with a larger halo spin (see Fig. 3 in Long et al. 2014).

A2 Initial Q value

To verify the expectation that the initial value of Toomre's Q parameter (Q_0) influences the bar and spiral structure, we created a set of models in which we varied this parameter.

The models are based on md0.5mb0, with one having an initially unstable disk (md0.5mb0Q0.5) and the other having a large Q_0, in which no spiral arms develop (md0.5mb0Q2.0). The time evolution of the bar's amplitude and length is presented in Fig. A7 and the surface densities are shown in Fig. A8. For md0.5mb0Q2.0 there is no sign of spiral or bar structure until $\sim 5\,\mathrm{Gyr}$, but a bar develops shortly after that (left panel of Fig. A7). This matches with the expectation that Q_0 influences the bar formation epoch, the smaller the Q_0 value the faster the bar forms. The peak amplitude just after the bar formation is higher for the larger Q_0, but the final amplitude is similar (see the left panel of Fig. A7). We also confirmed that the final bar length does not depend on Q_0 (see the right panel of Fig. A7). However, the radius that gives the maximum amplitude is different for the models with a large or a small value of Q. The radius for $A_{2,\mathrm{max}}$ is 2.6 and 4.9 kpc for models with $Q_0 = 0.5$ and 2.0, respectively. This result is qualitatively consistent with Hozumi (2012) where an initially colder disk forms a weaker and more compact bar due to the smaller velocity dispersion of the disk (although they stopped their simulation just after the first amplitude peak).

This further proves (as discussed in Section 3.3) that the growth rate of swing amplification governs the bar formation timescale. The growth rate decreases as Q increases (Toomre 1981) which is confirmed by our simulations. With $Q_0 = 2.0$, the disk is initially stable and hence the spiral structure has to be induced by the bar. These ring-like spiral arms are sometimes seen in SB0–SBa galaxies such as NGC 5101 (Ho et al. 2011).

A3 Disk scale length

We further examine models md1mb1Rd1.5 and md0.5mb1Rd1.5, which have a larger disk length scale. For these models the total disk mass is the same as that of
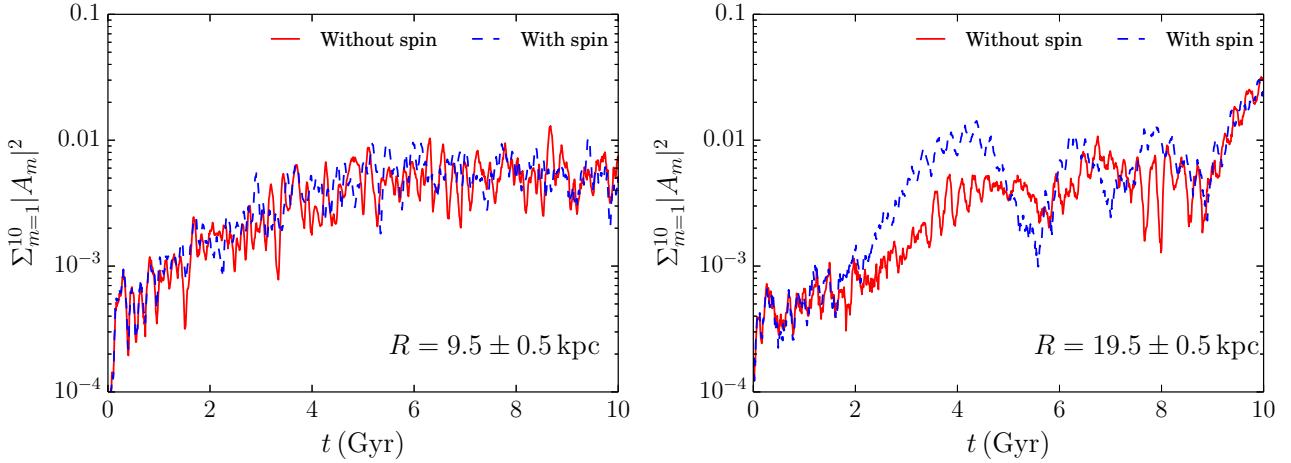
Figure A4. Total power for models md0.5Rd1.5 and md0.5Rd1.5s at $R = 9.5$ kpc (left) and 19.5 kpc (right).

models md1mb1 and md0.5mb1, but the disk scale length is larger. The changed disk scale length results in different rotation curves (see Fig. A9). Given Eq. 9 we expect that this leads to fewer spiral arms. The top views of these models are presented in Fig. A9 (right panels) and the evolution of the bar's amplitude and length in Fig. A10. The bar formation epoch of model md1mb1Rd1.5 (2 Gyr) is later than that of model mdmb1 (1 Gyr). Model md0.5mb1Rd1.5 did not form a bar within 10 Gyr, although model md0.5mb1 formed a bar at ∼ 6 Gyr. The difference between these models is that the disk mass fraction (f_d) for model md1mb1R1.5 and md0.5mb1R1.5 is smaller than those for model md1mb1 and md0.5mb1 (see Table 4). Although the bar formation starts later for model md1mb1Rd1.5, the bar grows faster, and the final bar length at 10 Gyr is comparable for these models. The bar's secular evolution, however, may continue further. In order to understand what decides the final bar length further simulations are required.

APPENDIX B: EVOLUTION OF SPIRAL ARMS IN A LIVE HALO

For the formation and evolution of bars, the effect of a live halo has been investigated in previous work, and it has been shown that the angular-momentum transfer from bars to live halos helps the growth of bars (Debattista & Sellwood 2000; Athanassoula 2002, 2003). Previous work, however, focused on the evolution of bars but not on spiral arms. In most of the previous work rigid halo simulations were used to study the dynamical evolution of spiral arms. As all our simulations are performed using a live halo, we made a comparison to the results in Fujii et al. (2011) to test the effect of a live halo on the spiral structure.

In Fig. B1 the relation between Q and the total amplitude ($\sum_{m=1}^{20} |A_m|^2$) at $t = 0, 0.125, 2.5, 5$, and 10 Gyr is presented for our models at $R = 2.2R_d$. The left panel shows the models which did not form a bar until 10 Gyr. In Fujii et al. (2011) we found that the spiral amplitudes grow up to a maximum given by the following equation:

$$A_m = 3.5C - 1.0 - 0.75Q^2, \qquad (B1)$$

where C depends on the shape of the spiral arms. Following Fujii et al. (2011), we use $C = 3/5$ because we assume that the local density enhancement due to spiral formation is described by the collapse of a homogeneous sphere. If we consider that $|A_m|^2$ is similar to the total amplitude, then the amplitudes of self-gravitating spiral arms can be analytically obtained as a function of Q. Fujii et al. (2011) further found that after the spiral arm has reached its maximum amplitude, Q increases because of the heating of the spiral arms and, following equation B1, the amplitude starts to decay (black curve in Fig. B1). For models without a bar we obtain the same results as for our models with live halos, although most of the data points are from before the amplitude decrease (see the left panel of Fig. B1). Results for bar forming models are shown in the right panel of Fig. B1. Before bar formation (small symbols), the relation between the amplitude and Q is similar to that in spiral galaxies, i.e., the amplitude is smaller than the maximum predicted amplitude (black curve). There are three points which exceed the limit, which was also seen in Fujii et al. (2011). After the bar forms, the developed amplitudes exceed that of the maximum given by Q, this is indicated by the larger symbols in the figures. The symbols are clearly above the theoretical line and Q keeps increasing due to the bar induced heating.

Snapshots of the bar models indicate that in the outer regions of the disk the spiral structure seems to disappear after the bar evolves (see Figs. 3 and A3), but the Fourier amplitudes are still large compared to the models without bars, as shown in Fig. B1. In the right panel we see that the amplitude tends to decrease as Q increases i.e., as the secular evolution proceeds, except for models md1mb1, md1mb1Rd1.5, and md0.5mb0, where the length of the bar reaches the reference radius ($2.2R_d$) by 10 Gyr. In these models, we take the amplitude of the bar as the total amplitude because the amplitude at $m = 2$ is much larger than the others. For these models, the relation between Q and the spiral amplitude is not applicable at $2.2R_d$ because the bar extends to this distance. Therefore, we also see that, even for barred spiral models, the spiral amplitude decreases as Q increases. The measured spiral amplitude, however, is much larger compared to the amplitude for spiral only models.

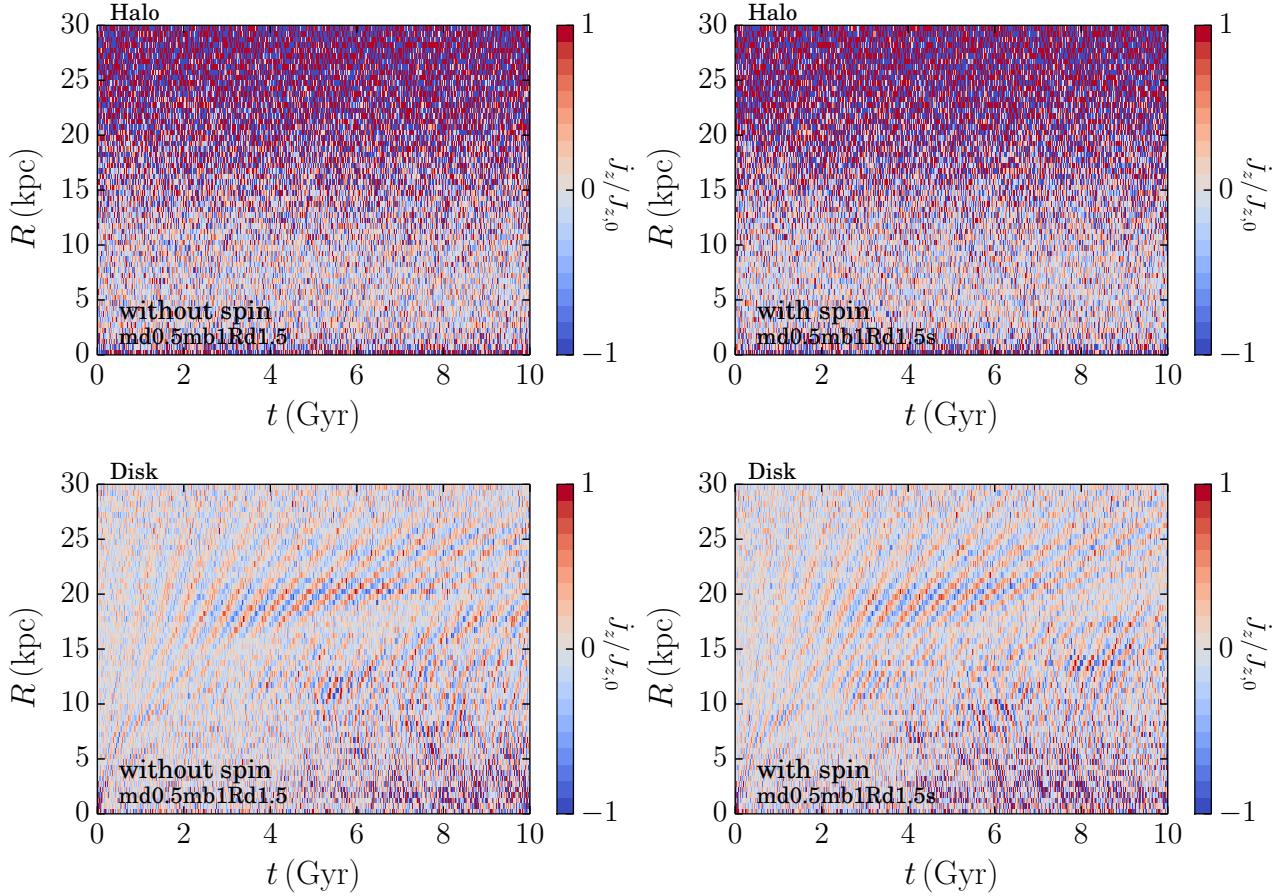The distribution of Q as a function of the galactic ra-

Figure A5. Angular momentum flow of the halo (top) and the disk (bottom) as a function of cylindrical radius and time for models md0.5mb1Rd1.5 (left) and md0.5mb1Rd1.5s (right). The angular momentum flow is calculated from the angular momentum's change in the *z*-component for every $\sim 10\,\mathrm{Myr}$. The value (color) is scaled to the initial angular momentum of the disk at each radius for both the disks and halos.
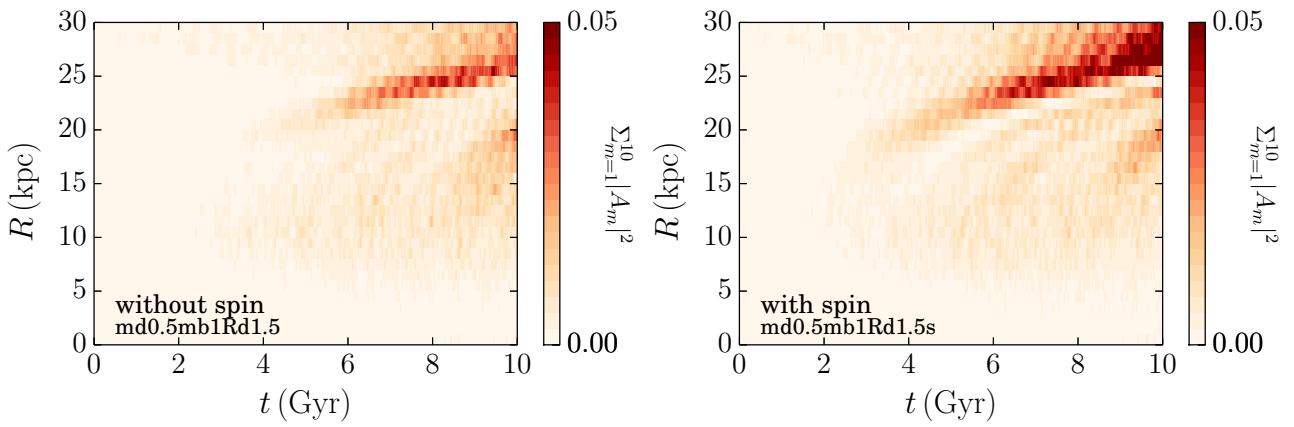

Figure A6. Total power as a function of cylindrical radius and time for models md0.5Rd1.5 (left) and md0.5Rd1.5s (right).

dius for models md1mb1 (strong bar) and md0.5mb4 (without bar, although a bar forms after $10\,\mathrm{Gyr}$) is presented in Fig. B2. The spiral arms heat up the disk moderately (left panel), but the bars heat up the disk dramatically once they are formed (right panel).

Another effect of the bar is that it seems to prevent the

formation of self-gravitating spiral arms, which corresponds to the number of spiral arms expected from swing amplification. In Fig. B3, the expected number of spiral arms (m_X) for model md1mb1 at $t = 1.25$, 2.5, 5, and $10\,\mathrm{Gyr}$ is presented. In the outer regions of the disk, m_X decreases as the bar develops, but still $m_X > 2$. However, when measured us-
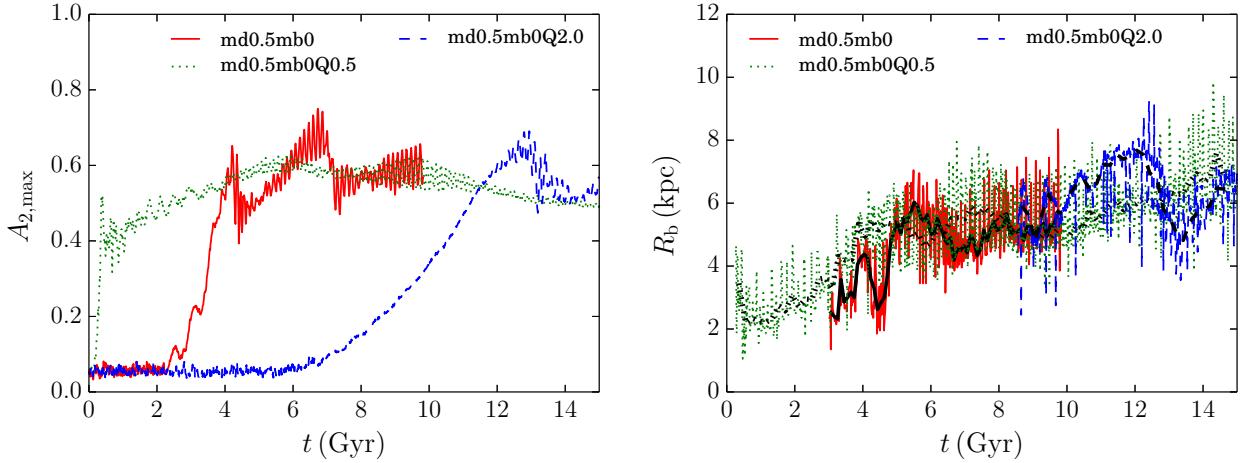
Figure A7. Same as Fig. 7, but for models md0.5mb0Q0.5 and md0.5mb0Q2.0.
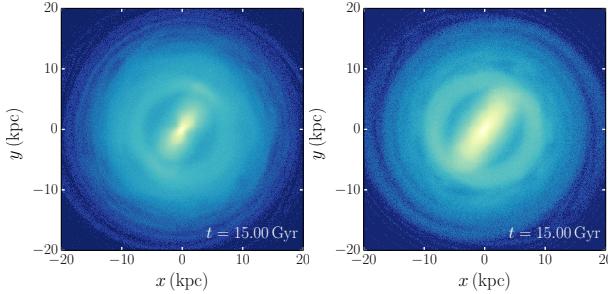

Figure A8. Snapshots for models md0.5mb0Q0.5 (left) and md0.5mb0Q2.0 (right).
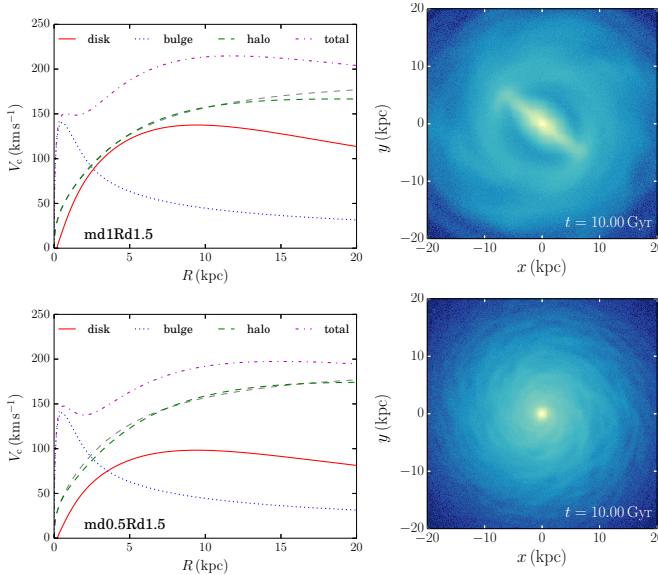

Figure A9. Rotation curves (left) and snapshots at 10 Gyr (right) for models md1mb1Rd1.5 (top) and md0.5mb1Rd1.5 (bottom). The gray dashed curve is the same as the one in Fig. 12.

ing Fourier decomposition (Eq. (10)) we always find $m = 2$ after bar formation (see also md1mb1 in Fig. 3). One possible reason for this is that the high Q value prevents the formation of self-gravitating spiral arms after the bar has formed, even though it is known that the bar induces spirals. In real galaxies, we often see multiple spiral arms in the bar's outer region. This discrepancy may be because our simulations ignore the effect of gas.

To conclude, using a live halo instead of an analytic halo potential is important when studying the formation and evolution of the bar and its properties in disk galaxies. Since the live halo influences the angular momentum of the bar, its speed and length will be rather different than when an analytic halo is adopted. The effect on spiral structure without a bar, however, is less pronounced.

APPENDIX C: RELATION BETWEEN BULGE-TO-DISK MASS RATIO AND SHEAR RATE

In Section 3.4 we showed that the bulge-to-disk mass ratio (B/D) is not always a good indicator for the shear rate (Γ), because Γ also depends on other parameters such as the disk-mass fraction ($f_{\rm d}$). Here, we construct additional initial conditions by sequentially changing some parameters in order to investigate their importance. We do not simulate these models, but measure B/D and Γ in the generated models at $t = 0$. All parameters of these models are summarized in Tables C1 and C2.

In Fig. C1, we present the relation between B/D and Γ calculated from the additional initial conditions. If we keep both $f_{\rm d}$ and the bulge scale length ($r_{\rm b}$) constant, Γ monotonically increases as B/D increases (square symbols). But if we increase $r_{\rm b}$ while keeping $f_{\rm d}$ constant, then Γ also increases (triangle symbols). If we increase $f_{\rm d}$ and keep B/D and $r_{\rm b}$ constant, Γ increases (diamond symbols). The halo scale length ($r_{\rm h}$) and scale velocity ($\sigma_{\rm h}$), on the other hand, barely affect the relation between B/D and Γ (circle symbols).
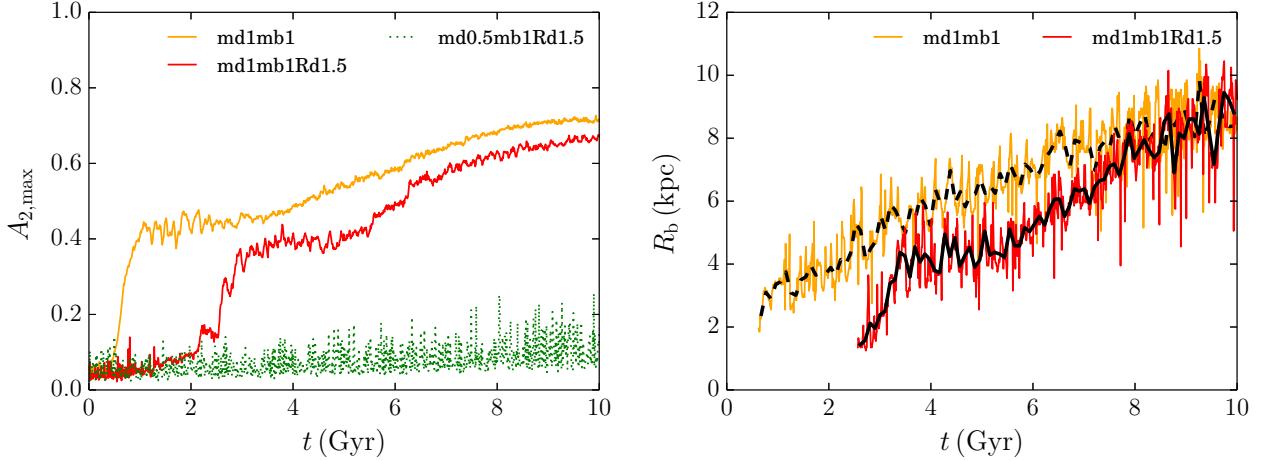
Figure A10. Same as Fig. 7, but now for models md1mb1Rd1.5 and md0.5mb1Rd1.5 with md1mb1 shown as reference.
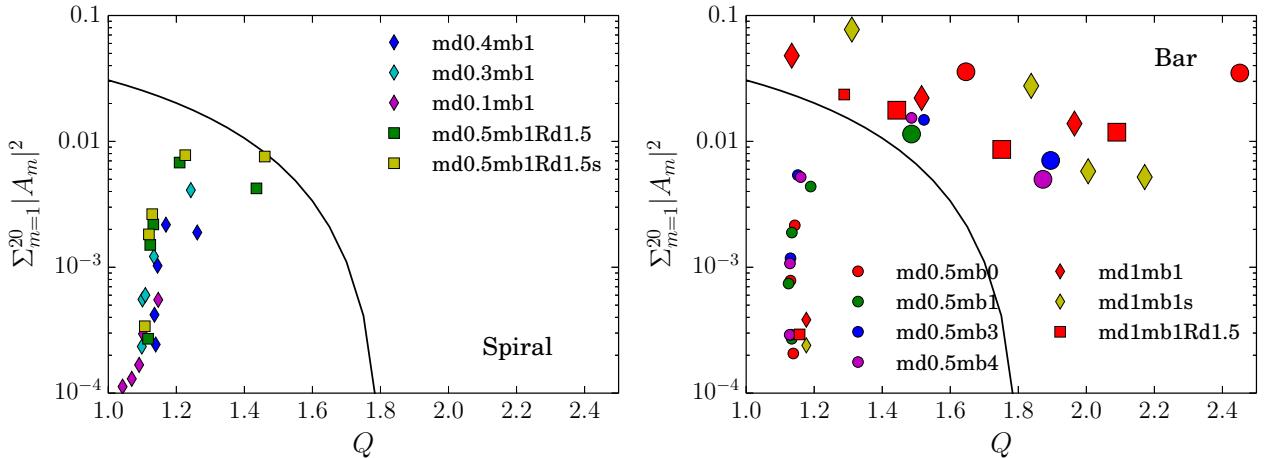

Figure B1. Relation between Q and the total power of the Fourier amplitudes at the reference radii ($R = 6.5 \pm 0.5\,\mathrm{kpc}$, except for models md1mb1Rd1.5, md0.5mb1Rd1.5 and md0.5mb1Rd1.5s where $R = 9.5 \pm 0.5\,\mathrm{kpc}$) at $t = 0, 0.125, 2.5, 5,$ and $10\,\mathrm{Gyr}$. Large symbols indicate the data points from after the bar formation. The total power is averaged over 20 snapshots ($\sim 200\,\mathrm{Myr}$). Black curves indicate Eq. B1 for $|0.1A_\mathrm{m}|^2$. We adopt this value in order to compare with Fig. 12 in Fujii et al. (2011).
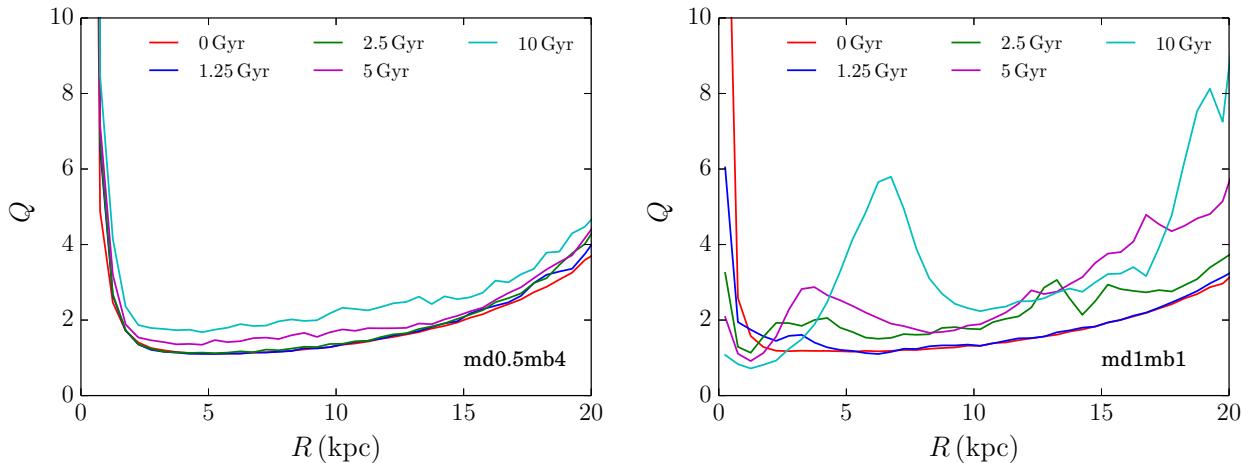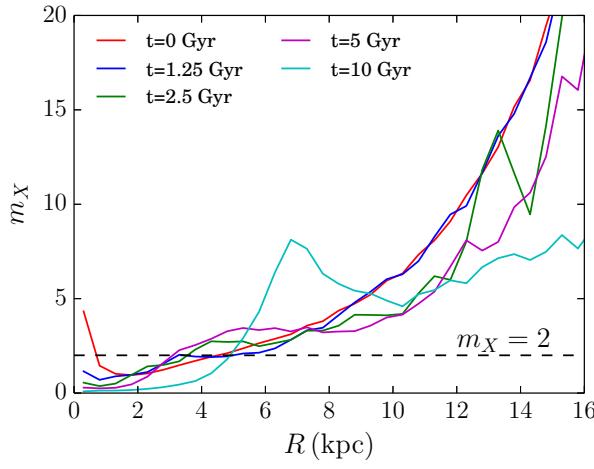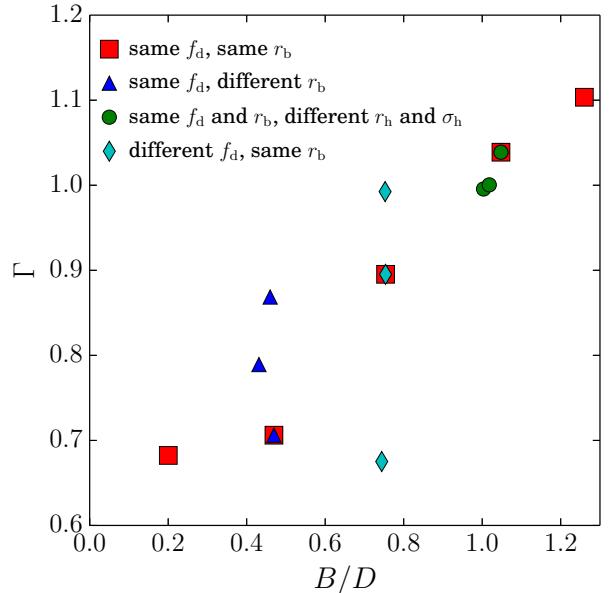

Figure B2. Time evolution of Toomre's Q for models md0.5mb4 (left) and md1mb1 (right). The peak in the cyan curve at $R \sim 7\mathrm{kpc}$ corresponds to the end of the bar.

Table C1. Parameters for additional initial conditions

	Halo			Disk				Bulge		
Parameters Model	$a_{\rm h}$ (kpc)	$\sigma_{\rm h}$ (km s^{-1})	$1-\varepsilon_{\rm h}$	$M_{\rm d}$ ($10^{10}M_\odot$)	$R_{\rm d}$ (kpc)	$z_{\rm d}$ (kpc)	σ_{R0} (km s^{-1})	$a_{\rm b}$ (kpc)	$\sigma_{\rm b}$ (km s^{-1})	$1-\varepsilon_{\rm b}$
Add1	8.2	350	0.9	2.45	2.8	0.36	105	0.64	300	1.0
Add2	11.5	443	0.9	2.45	2.8	0.36	105	0.65	400	1.0
Add3	8.2	370	0.9	2.45	2.8	0.36	105	0.64	500	1.0
Add4	10	340	0.9	2.45	2.8	0.36	105	0.64	550	1.0
Add5	8.2	295	0.9	2.45	2.8	0.36	105	0.65	600	1.0
Add6	8.2	284	0.9	2.45	2.8	0.36	105	1.3	370	1.0
Add7	8.2	330	0.9	2.45	2.8	0.36	105	0.8	380	1.0
Add8	8.2	330	1.0	2.45	2.8	0.36	105	0.64	550	1.0
Add9	12	400	1.0	2.45	2.8	0.36	105	0.64	540	1.0
Add10	8.2	370	0.9	1.47	2.8	0.36	105	0.64	390	1.0
Add11	12	330	0.9	2.45	2.8	0.36	105	0.64	486	1.0

Table C2. Obtained values for additional initial conditions

Model	$M_{\rm d}$ ($10^{10}M_\odot$)	$M_{\rm b}$ ($10^{10}M_\odot$)	$M_{\rm h}$ ($10^{10}M_\odot$)	$M_{\rm b}/M_{\rm d}$ (kpc)	$R_{\rm d,t}$ (kpc)	$r_{\rm b,t}$ (kpc)	$r_{\rm h,t}$	$f_{\rm d}$	Γ
Add1	2.57	0.514	56.0	0.20	31.6	3.57	284	0.346	0.682
Add2	2.58	1.21	137	0.47	31.6	5.32	330	0.343	0.706
Add3	2.69	2.03	94.6	0.75	31.6	6.65	234	0.321	0.895
Add4	2.59	2.74	124	1.05	31.6	8.67	288	0.340	1.04
Add5	2.61	3.29	93.2	1.26	31.6	9.48	270	0.307	1.10
Add6	2.59	1.19	45.9	0.46	31.6	6.28	265	0.332	0.869
Add7	2.58	1.11	61.3	0.43	31.6	5.31	251	0.348	0.789
Add8	2.61	2.62	108	1.0	31.6	7.98	494	0.322	0.996
Add9	2.59	2.64	195	1.02	31.6	8.46	687	0.341	1.00
Add10	1.58	1.18	74.8	0.74	31.6	5.65	234	0.251	0.675
Add11	2.75	2.07	130	0.75	31.6	8.00	324	0.401	0.992

Figure B3. The number of spiral arms using Eq. 9 at $t = 0$, 0.125, 0.25, 5, and 10 Gyr for model md1mb1. The peak in the cyan curve at $R \sim 7$ kpc corresponds to the bar end.

Figure C1. Relation between bulge-to-disk mass ratio (B/D) and shear rate (Γ).

REFERENCES

Abadi M. G., Navarro J. F., Steinmetz M., Eke V. R., 2003, ApJ, 591, 499

Athanassoula E., 1984, Phys. Rep., 114, 319
Athanassoula E., 2002, ApJ, 569, L83
Athanassoula E., 2003, MNRAS, 341, 1179
Athanassoula E., 2008, MNRAS, 390, L69
Athanassoula E., Sellwood J. A., 1986, MNRAS, 221, 213
Baba J., 2015, MNRAS, 454, 2954
Baba J., Saitoh T. R., Wada K., 2013, ApJ, 763, 46
Barnes J., Hut P., 1986, Nature, 324, 446
Bédorf J., Gaburov E., Portegies Zwart S., 2012, Journal of Computational Physics, 231, 2825
Bédorf J., Gaburov E., Fujii M. S., Nitadori K., Ishiyama T., Portegies Zwart S., 2014, in Proceedings of the International Conference for High Performance Computing, Networking, Storage and Analysis, p. 54-65. pp 54–65 (arXiv:1412.0659), doi:10.1109/SC.2014.10OTHER: http://dl.acm.org/citation.cfm?id=2683600
Binney J., Tremaine S., 2008, Galactic Dynamics: Second Edition. Princeton University Press
Bottema R., 2003, MNRAS, 344, 358
Carlberg R. G., Freedman W. L., 1985, ApJ, 298, 486
Combes F., Debbasch F., Friedli D., Pfenniger D., 1990, A&A, 233, 82
D'Onghia E., 2015, ApJ, 808, L8
Debattista V. P., Sellwood J. A., 2000, ApJ, 543, 704
Dobbs C., Baba J., 2014, PASA, 31, 35
Dubinski J., Berentzen I., Shlosman I., 2009, ApJ, 697, 293
Efstathiou G., Lake G., Negroponte J., 1982, MNRAS, 199, 1069
Elmegreen D. M., Elmegreen B. G., 1982, MNRAS, 201, 1021
Fujii M. S., Baba J., Saitoh T. R., Makino J., Kokubo E., Wada K., 2011, ApJ, 730, 109
Genzel R., et al., 2017, Nature, 543, 397
Goldreich P., Lynden-Bell D., 1965, MNRAS, 130, 125
Grand R. J. J., Kawata D., Cropper M., 2013, A&A, 553, A77
Hernquist L., 1990, ApJ, 356, 359
Ho L. C., Li Z.-Y., Barth A. J., Seigar M. S., Peng C. Y., 2011, ApJS, 197, 21
Hohl F., 1971, ApJ, 168, 343
Hozumi S., 2012, PASJ, 64, 5
Hubble E. P., 1926, ApJ, 64, 321
Iannuzzi F., Athanassoula E., 2013, MNRAS, 436, 1161
Julian W. H., Toomre A., 1966, ApJ, 146, 810
Kendall S., Kennicutt R. C., Clarke C., 2011, MNRAS, 414, 538
Kormendy J., Norman C. A., 1979, ApJ, 233, 539
Kunder A., et al., 2012, AJ, 143, 57
Lin C. C., Shu F. H., 1964, ApJ, 140, 646
Long S., Shlosman I., Heller C., 2014, ApJ, 783, L18
Michikoshi S., Kokubo E., 2014, ApJ, 787, 174
Michikoshi S., Kokubo E., 2016a, ApJ, 821, 35
Michikoshi S., Kokubo E., 2016b, ApJ, 823, 121
Navarro J. F., Frenk C. S., White S. D. M., 1997, ApJ, 490, 493
Okamoto T., Isoe M., Habe A., 2015, PASJ, 67, 63
Ostriker J. P., Peebles P. J. E., 1973, ApJ, 186, 467
Peebles P. J. E., 1969, ApJ, 155, 393
Peebles P. J. E., 1971, A&A, 11, 377
Pettitt A. R., Wadsley J. W., 2018, MNRAS, 474, 5645
Portegies Zwart S., Bédorf J., 2015, Computer, 48, 50
Portegies Zwart S., McMillan S., 2018, Astrophysical Recipes: the Art of AMUSE. AAS IOP Astronomy
Saha K., Naab T., 2013, MNRAS, 434, 1287
Sandage A., 1961, The Hubble Atlas of Galaxies
Scannapieco C., Athanassoula E., 2012, MNRAS, 425, L10
Schwarz M. P., 1981, ApJ, 247, 77
Seigar M. S., 2005, MNRAS, 361, L20
Seigar M. S., Bullock J. S., Barth A. J., Ho L. C., 2006, ApJ, 645, 1012
Sellwood J. A., Carlberg R. G., 1984, ApJ, 282, 61
Sellwood J. A., Carlberg R. G., 2014, ApJ, 785, 137
Sellwood J. A., Debattista V. P., 2009, MNRAS, 398, 1279

Sellwood J. A., Evans N. W., 2001, ApJ, 546, 176
Shen J., Rich R. M., Kormendy J., Howard C. D., De Propris R., Kunder A., 2010, ApJ, 720, L72
Shlosman I., Noguchi M., 1993, ApJ, 414, 474
Steinmetz M., Navarro J. F., 2002, New A, 7, 155
Tempel E., Tenjes P., 2006, MNRAS, 371, 1269
Toomre A., 1964, ApJ, 139, 1217
Toomre A., 1981, in Fall S. M., Lynden-Bell D., eds, Structure and Evolution of Normal Galaxies. pp 111–136
Toomre A., Toomre J., 1972, ApJ, 178, 623
Villa-Vargas J., Shlosman I., Heller C., 2009, ApJ, 707, 218
Widrow L. M., Dubinski J., 2005, ApJ, 631, 838
Widrow L. M., Pym B., Dubinski J., 2008, ApJ, 679, 1239
Zasov A. V., Moiseev A. V., Khoperskov A. V., Sidorova E. A., 2008, Astronomy Reports, 52, 79
de Vaucouleurs G., 1959, Handbuch der Physik, 53, 275